Discriminating electroweak-ino parameter ordering at the LHC and its impact on LFV studies

Discriminating electroweak-ino parameter ordering at the LHC and its impact on LFV studies

Junji Hisano,[a,b] **Mihoko M. Nojiri**[b,c,d] **and Warintorn Sreethawong**[c,d]

[a]*Institute for Cosmic Ray Research (ICRR), University of Tokyo,*
Kashiwa, Chiba 277-8582, Japan

[b]*IPMU, Tokyo University,*
Kashiwa, Chiba, 277-8568, Japan

[c]*Theory Group, KEK,*
1-1 Oho, Tsukuba, Ibaraki 305-0801, Japan

[d]*The Graduate University for Advanced Studies (Sokendai),*
1-1 Oho, Tsukuba, Ibaraki 305-0801, Japan

E-mail: hisano@icrr.u-tokyo.ac.jp, nojiri@post.kek.jp,
warinto@post.kek.jp

ABSTRACT: Current limit on the dark matter relic abundance may suggest that $|\mu|$ should be smaller than prediction in the minimal supergravity scenario (mSUGRA) for moderate m_0 and $m_{1/2}$. The electroweak-ino parameter M_1, M_2 and $|\mu|$ are then much closer to each other. This can be realized naturally in the non-universal Higgs mass model (NUHM). Since the heaviest neutralino ($\tilde{\chi}_4^0$) and chargino ($\tilde{\chi}_2^\pm$) have significant gaugino components, they may appear frequently in the left-handed squark decay and then be detectable at the LHC. In such a case, we showed that the hierarchy of M_1, M_2 and $|\mu|$ can be determined. In the light slepton mass scenario with non-vanishing lepton-flavor violation (LFV) in the right-handed sector, NUHM with small $|\mu|$ corresponds to region of parameter space where strong cancellation among leading contributions to $Br(\mu \to e\gamma)$ can occur. We showed that determination of electroweak-ino hierarchy plays a crucial role in resolving cancellation point of $Br(\mu \to e\gamma)$ and determination of LFV parameters. We also discussed test of the universality of the slepton masses at the LHC and the implications to SUSY flavor models.

Contents

1 Introduction

Even though the Standard Model (SM) describes the Nature very well, there are a number of theoretical and phenomenological issues that the SM cannot give a plausible explanation. The notorious one is the hierarchy problem. In the absence of a symmetry to protect the mass of the Higgs boson from the radiative corrections, its natural value should be of order of UV cutoff scale. However, from the precision electroweak measurements, the SM Higgs mass is lower than $193\,\mathrm{GeV}$ at the 95% confidence level [1]. On the cosmological side, while the evidence of the dark matter (DM) in the universe is now available from a variety of observational data [2–7], the SM cannot provide a viable candidate for it. Therefore, it is convincing that the SM must be viewed as a low energy effective theory of the more fundamental theory.

Supersymmetry (SUSY) is one among the most promising candidates of the physics beyond the SM. It provides a natural solution to the hierarchy problem and allows the unification of gauge couplings in the context of grand unified theory (GUT). Moreover, in the model with conserved R-parity, the lightest supersymmetric particle (LSP), typically the lightest neutralino, is stable and provides a dark matter candidate.

In general SUSY models, the non-vanishing off-diagonal elements of the slepton mass violate the lepton-flavor conservation and then are strongly constrained by experiments [8]. Since arbitrary sfermion masses generally lead to flavor-changing-neutral-current (FCNC) processes exceeding the experimental bounds, universality among generation of sfermion masses is usually imposed at some high energy scale. The most popular one is the minimal supergravity scenario (mSUGRA) [9], whose input parameters are the universal scalar mass m_0, the universal trilinear scalar coupling A_0, the gaugino mass $m_{1/2}$ at the GUT scale and $\tan\beta$.

Only small regions of mSUGRA parameter space have DM relic density within the observational bound [10]. This is because $|\mu| \gg m_{1/2}$ is predicted for moderate $m_0 \sim m_{1/2}$ and the LSP is almost pure Bino in this scenario. For moderate $\tan\beta$, only t-channel $\tilde{l}_R$ exchange diagram gives important contribution to DM annihilation cross section [11]. Therefore, the cross section is typically too small and the relic abundance exceeds the experimental upper bound. However, when relaxing the universality condition of the SUSY breaking parameters at the GUT scale, one can freely adjust the thermal relic density.

One of the well-motivated relaxations is to allow soft scalar Higgs masses to be varied such as in the non-universal Higgs mass model (NUHM) [12–15].

Supersymmetric particles may be discovered in the early stages of LHC data collection. The squarks and gluino with masses below $1.5\,\mathrm{TeV}$ are expected to be found at the LHC for $\mathcal{L} = 1\ \mathrm{fb}^{-1}$ at $\sqrt{s} = 14\,\mathrm{TeV}$ [16]. By studying the kinematics of long cascade decays, one can extract information on masses of sparticles involved and more or less constrain the parameter space of the underlying theory. This is especially successful when sleptons are involved in the cascade decays. However, it was pointed out that, for a given set of experimental SUSY signatures at the LHC, more than one set of parameters could be present and ambiguities predominantly occur in the electroweak-ino sector. This is sometimes called the LHC Inverse Problem [17]. A similar result was obtained in [18] when an exclusive likelihood map of SPS1a point is studied by a weighted Markov chain technique. Even for the favorable SPS1a point, we have multiple solutions.

In this paper, we study the interplay between the LHC measurements of the parameters in electroweak (EW) sector and lepton-flavor violation. The LFV processes are important discovery channels of physics beyond the standard model. Right now, the main constraints come from the upper bounds of rare decay process searches [19–21]:

$$Br(\mu \to e\gamma) < 1.2 \times 10^{-11}, \tag{1.1}$$

$$Br(\tau \to \mu\gamma) < 4.5(6.8) \times 10^{-8}, \tag{1.2}$$

$$Br(\tau \to e\gamma) < 1.2(1.1) \times 10^{-7}. \tag{1.3}$$

The bounds for tau LFV processes come from Belle (Babar). On-going MEG experi-

ment [22] aims to push the sensitivity of $\mu \to e\gamma$ down by two orders of magnitude, and the SuperKEKB [23] and SuperB Factory [24] aim to improve the sensitivity of the τ decay by one or two orders of magnitude in near future.

If slepton is directly observed at the LHC, together with these advanced LFV measurements, we will be able to study the flavor sector of supersymmetry in detail. Several papers [15, 25, 26] recently point out that the ability of the LHC to measure the slepton mass differences will significantly constrain the possible scenarios. The further improvement may be obtained through the constraints on U(1) and SU(2) gaugino masses, M_1 and M_2, and μ parameter from the neutralino and chargino mass measurements at the LHC. Note that the inverse problem has an impact on the $\mu \to e\gamma$ study. As will be discussed in detail later, the $Br(\mu \to e\gamma)$ could be suppressed due to cancellation among different diagrams [27]. The severity of the cancellation depends strongly on value of μ parameter and slepton masses. Accordingly, to unravel the off-diagonal elements from the measurement of rare decay processes such as $Br(\mu \to e\gamma)$, one needs to solve the inverse problem and determine the SUSY parameters precisely.

In this paper, we take the non-universal Higgs mass model with positive μ with $\mu \sim m_{1/2}$ due to the DM relic abundance reason. In addition, we choose a mass hierarchy $m_{\tilde{\chi}_1^0} < m_{\tilde{e}_R} < m_{\tilde{\chi}_2^0} < m_{\tilde{e}_L} < m_{\tilde{\chi}_4^0}$ so that both left- and right-handed sleptons appear in neutralino decay. Notably, we find $m_{\tilde{e}_R} < m_{\tilde{\chi}_2^0}$ and $m_{\tilde{e}_L} < m_{\tilde{\chi}_4^0}$ should be satisfied when there is strong cancellation among the LFV diagrams involving the right-handed sleptons for the model points with correct DM relic abundance in the NUHM. For this parameters, many cascade decay modes involving sleptons can be observed at the LHC. Using the information, a solution of the EW parameters can be selected among the multiple solutions, and ambiguity in the MSSM parameters would be reduced significantly, leading better prediction to $Br(\mu \to e\gamma)$ from the LFV slepton masses.

The paper is organized as follows. In the next section, we introduce models we study. The sparticle mass determination is studied by explicit MC simulation in section III for our sample model point. In section IV, we discuss the ambiguity of the corresponding MSSM parameters and demonstrate that it can be removed by studying decay branching ratios of $\tilde{\chi}_i \to 2l + X$, charge asymmetry of the decay distribution, and the rate into 2 hard jets + missing E_T mode at the LHC. The implication to LFV studies is discussed in section V. We emphasize the importance of the slepton masses determination and compare the sensitivity to the off-diagonal elements of slepton mass matrices at the LHC and the other LFV searches such as MEG experiments. We also study the relation among slepton masses and μ parameter at the point of $Br(\mu \to e\gamma)$ cancellation. We show that the MSSM parameters would be studied very precisely at the LHC through the cascade decays involving sleptons. Finally, section VI is devoted to discussions.

2 Models

The models under consideration in this paper consist of two important features. The first one is related to the scale of sparticle masses and their hierarchy. We chose the NUHM model as a representative. The second class involves issue of lepton-flavor-violation. Here,

two models are selected: the MSSM with right-handed neutrinos and the MSSM with horizontal symmetry. Although models of interest have both NUHM and LFV, the detail descriptions of these features are given separately below.

2.1 Non-universal Higgs mass model

This model is motivated by the supersymmetric grand unified theories in which the Higgs fields do not belong to the same multiplet as the matter fields. Therefore, it is natural to expect that different multiplets would have different soft masses at the GUT scale.

In mSUGRA scenario, for the correct pattern of EWSB, $m_{H_U}^2 + \mu^2 > -m_Z^2/2$ must be satisfied at weak scale. Since the SUSY breaking mass squared for the Higgs doublet H_U, $m_{H_U}^2$, is always driven to large negative value at weak scale by large top Yukawa coupling, $|\mu|$ is typically large. A smaller $|\mu|$ value can be easily obtained if one relaxes universality condition, especially $m_{H_U} > m_0$ at the GUT scale. Once $|\mu| \sim m_{1/2}$, the LSP has larger Higgsino components. In that case, s-channel Z/h^0 exchange contributions and $\tilde{\chi}_1^0 \tilde{\chi}_1^0 \to WW$ contribution to the DM pair-annihilation cross section become more important [11, 28] and the relic abundance would be small to be compatible with observational value.

On the collider physics side, the reduction of $|\mu|$ would lead to a rich pattern of colored sparticle cascade decays at the LHC. Due to their considerable Wino components, $\tilde{\chi}_4^0$ and $\tilde{\chi}_2^\pm$ can be produced copiously in SU(2) doublet squark decay. Their successive cascade decays are the followings [14]:

$$
\begin{aligned}
\tilde{\chi}_2^+ &\to \tilde{\nu}_L \to \tilde{\chi}_1^+\,, \\
\tilde{\chi}_4^0 &\to \tilde{l}_R \to \tilde{\chi}_1^0\,, \\
\tilde{\chi}_4^0 &\to \tilde{l}_L \to \tilde{\chi}_2^0, \tilde{\chi}_1^0\,,
\end{aligned}
\tag{2.1}
$$

which lead to clean, fruitful opposite sign same flavor (OSSF) dilepton events. The maximum values of dilepton invariant mass distributions depend on the cascade decay chains. If several endpoints can be identified and measured, it gives access to sparticle masses, or at least, their mass differences.

2.2 LFV models

In the MSSM the low-energy LFV processes are induced by the off-diagonal terms in the slepton mass matrices, which depend on the origin of the SUSY breaking and physics beyond the MSSM. In this paper we discuss two models which predict LFV, i) MSSM with right-handed neutrinos and ii) MSSM with horizontal symmetries.

Before going to those models, we first discuss $\mu \to e\gamma$ process and an anomalous magnetic dipole moment $a_{l_j} \equiv (g-2)_{l_j}$. The effective operators for $l_j^- \to l_i^- \gamma$ and a_{l_j} are written as

$$
\mathcal{L}_{\text{eff}} = e \frac{m_{l_j}}{2}\, \bar{l}_j \sigma^{\mu\nu} F_{\mu\nu} (A_{ij}^L P_L + A_{ij}^R P_R) l_i
\tag{2.2}
$$

where m_{l_j} is a mass of the charged lepton l_j. The coefficients A_{ij}^L and A_{ij}^R are functions of masses and mixings of sparticles inside the loop corrections. Their full formula can be

found in [27]. The SUSY contributions to the anomalous magnetic dipole moment of the muon, a_μ^{SUSY}, is given by

$$a_\mu^{\text{SUSY}} = m_\mu^2 (A_{22}^L + A_{22}^R). \tag{2.3}$$

The branching ratio for the decay $l_j^- \to l_i^- \gamma$ is

$$Br(l_j^- \to l_i^- \gamma) = \frac{48\pi^3 \alpha}{G_F^2} (|A_{ij}^L|^2 + |A_{ij}^R|^2) \times Br(l_j^- \to l_i^- \bar{\nu}_i \nu_j). \tag{2.4}$$

The experimental value of the anomalous magnetic moment of the muon measured by the E821 experiment at Brookhaven with extremely high precision [29] is given by

$$a_\mu^{\text{exp}} = 116592080(63) \times 10^{-11}. \tag{2.5}$$

According to the most recent calculations of the hadronic contribution based on the $e^+ e^-$ data [30], the difference between the SM prediction and the experimental value is

$$\delta a_\mu = a_\mu^{\text{exp}} - a_\mu^{\text{SM}} = +302(88) \times 10^{-11}, \tag{2.6}$$

which corresponds to 3.4-σ deviations. It was pointed out that this discrepancy tends to come from new physics contributions as it is unlikely to be explained by errors in the determination of the hadronic contributions [31]. Moreover, in the context of SUSY, the δa_μ anomaly, eq. (2.6), suggests light slepton-chargino sector. Accordingly, unless flavor mixings are very small, $\mu \to e\gamma$ may be detected at MEG experiment [22] soon.

We now explain two LFV models and discuss their phenomenology.

2.2.1 MSSM with right-handed neutrinos

This model is motivated by the observations of non-vanishing neutrino masses and neutrino oscillation. In the model with three right-handed neutrinos, the superpotential for the lepton sector is given by

$$W = f_l^{ij} E_i^c L_j H_D + f_\nu^{ij} N_i^c L_j H_U + \frac{1}{2} M_\nu^{ij} N_i^c N_j^c, \tag{2.7}$$

where L_i, E_i^c and N_i^c represent chiral multiplets for left-handed lepton doublet, right-handed charged lepton singlet and right-handed neutrino singlet respectively, and H_U and H_D for two Higgs doublets with opposite hypercharge. The neutrino mass matrix can be obtained by the seesaw mechanism and is given by

$$m_\nu = f_\nu^T M_\nu^{-1} f_\nu \langle h_U \rangle^2 \tag{2.8}$$

where $\langle h_U \rangle$ is the vacuum expectation value of the neutral Higgs component h_U of the H_U multiplet.

In general, the Yukawa couplings f_l and f_ν cannot be diagonalized simultaneously. Therefore, even though one assumes that mass matrices for left-handed and right-handed

sleptons, $m_{\tilde{L}}^2$ and $m_{\tilde{e}}^2$, are proportional to the unit matrix at the GUT scale, the LFV masses of $m_{\tilde{L}}^2$ will always be generated via the renormalization group evolution,

$$\mu\frac{d}{d\mu}(m_{\tilde{L}}^2)_i^j = \left(\mu\frac{d}{d\mu}(m_{\tilde{L}}^2)_i^j\right)_{\text{MSSM}} + \frac{1}{16\pi^2}\left[(m_{\tilde{L}}^2 f_\nu^\dagger f_\nu + f_\nu^\dagger f_\nu m_{\tilde{L}}^2)_i^j\right.$$
$$\left.+2(f_\nu^\dagger m_{\tilde{L}}^2 f_\nu + \tilde{m}_{h_2}^2 f_\nu^\dagger f_\nu + A_\nu^\dagger A_\nu)_i^j\right],\quad(2.9)$$

by the non-vanishing off-diagonal elements of f_ν and of the trilinear soft parameter A_ν [32]. The large mixing angles observed in the atmospheric and solar neutrino oscillation experiments enhance the LFV masses of $m_{\tilde{L}}^2$, and the experimental bounds on $Br(\mu \to e\gamma)$ and $Br(\tau \to \mu\gamma)$ give stringent constraints on the model [33].

It has been studied that if the LFV is generated only in the left-handed slepton sector, $Br(\mu \to e\gamma)$ will be strongly correlated with $(a_\mu^{\text{SUSY}})^2$ [34]. This is because the chargino-sneutrino diagram dominates over other contributions in both observables. By taking a common mass for all sparticles, the current experimental bounds on $a_\mu^{\text{SUSY}}(\equiv \delta a_\mu)$ and $Br(\mu \to e\gamma)$ put a stringent constraint on the left-handed LFV slepton mass term,

$$\left|\frac{(m_{\tilde{L}}^2)_e^\mu}{m_{\text{SUSY}}^2}\right| \lesssim 2 \times 10^{-4} \left(\frac{|a_\mu^{\text{SUSY}}|}{3.02 \times 10^{-9}}\right)^{-1} \left(\frac{Br(\mu \to e\gamma)}{1.2 \times 10^{-11}}\right)^{\frac{1}{2}}.\quad(2.10)$$

On the other hand, we still have a room for sizable mass difference between the left-handed selectron and other sleptons, which may be measured at the LHC. Without LFV, basically the "left-handed" tau slepton mass is deviated from other left-handed slepton masses due to its Yukawa coupling effect to the renormalization group evolution or the left-right mixing term, while mass difference $m_{\tilde{e}_L} - m_{\tilde{\mu}_L}$ is negligibly small. However, in the case of nonzero LFV, mass splittings could be larger and would be detectable at the LHC.

2.2.2 MSSM with horizontal symmetry

Horizontal symmetries are introduced to derive the hierarchical structure in the Yukawa coupling constants [35] and also to suppress the off-diagonal terms in the sfermion mass matrices [36, 37].

In this paper, we studied the MSSM with horizontal symmetry, which is originated from one of models in [38]. The original model was a supersymmetric model in which the SUSY breaking is mediated to the MSSM by gravity interactions. The gravity-mediated contribution is assumed to be subject to an approximate horizontal symmetry. More specifically, consider a horizontal $U(1) \times U(1)$ symmetry where each $U(1)$ is explicitly broken by a scalar singlet spurion carrying the corresponding charge -1. The sizes of both $U(1)$ breakings are assumed to be equal and then parametrized by a single parameter $\epsilon \sim |V_{us}| \sim 0.2$. The horizontal charge assignment for lepton sector is as follows:

$$L_1(4,0),\qquad L_2(2,2),\qquad L_3(0,4);$$
$$\bar{E}_1(1,0),\qquad \bar{E}_2(1,-2),\qquad \bar{E}_3(0,-3).\quad(2.11)$$

Using above horizontal symmetry, we parameterize the left- and right-handed slepton mass matrices at the GUT scale as

$$m_{\widetilde{L}}^2 = m_0^2 + x m_0^2 X'_{\widetilde{L}}, \qquad M_{\widetilde{e}}^2 = m_0^2 + x m_0^2 X'_{\widetilde{e}}, \tag{2.12}$$

where x is the ratio between the flavor-independent and dependent contributions. The structure of matrices X'_L and X'_R can be determined uniquely by selection rules by the horizontal symmetry and have the following forms:

$$X'_{\widetilde{L}} \sim \begin{pmatrix} 0 & \epsilon^4 & \epsilon^8 \\ \epsilon^4 & 0 & \epsilon^4 \\ \epsilon^8 & \epsilon^4 & 0 \end{pmatrix}, \qquad X'_{\widetilde{e}} \sim \begin{pmatrix} 0 & \epsilon^2 & \epsilon^4 \\ \epsilon^2 & 0 & \epsilon^2 \\ \epsilon^4 & \epsilon^2 & 0 \end{pmatrix}. \tag{2.13}$$

Here, we neglect the flavor-dependent contribution to the flavor-diagonal mass terms, though they are also allowed by the symmetry with size $\sim x m_0^2$. It is argued in [38] that even $x \gtrsim 1$ is allowed from phenomenological constraints under the horizontal symmetry when $m_0 < 380\,\text{GeV}$, $m_{1/2} < 160\,\text{GeV}$, and $5 < \tan\beta < 15$.

To discuss the $\mu \to e\gamma$ phenomenology of this model, first of all, it should be remembered that the effective $\mu \to e\gamma$ operator, eq. (2.2), must flip the chirality and change the flavor of the external leptons. Since the left-handed LFV masses are suppressed in this model, the dominant LFV contribution comes from the right-handed sector. In the mass insertion approximation, there are two dominant one-loop diagrams when $M_1\mu\tan\beta$ is large [39]. The former one has chirality flip on an internal line via left-right slepton mixing and its contribution is

$$A_{12}^L\big|_{\widetilde{B}^0} = \frac{1}{2}\frac{\alpha_Y}{4\pi}\frac{1}{\overline{m}_{\widetilde{l}_R}^2}\frac{(m_{\widetilde{l}_R}^2)_e^\mu}{\overline{m}_{\widetilde{l}_R}^2}\frac{M_1(A_\mu + \mu\tan\beta)}{\overline{m}_{\widetilde{l}_L}^2}. \tag{2.14}$$

In the latter diagram, the chirality is flipped at one vertex via Yukawa coupling. The contribution is proportional to the Higgsino components, which come from the Bino-Higgsino mixing of neutralino. The amplitude is given by

$$A_{12}^L\big|_{(\widetilde{B}^0 - \widetilde{H}^0\text{mixing})} = -\frac{\alpha_Y}{4\pi}\frac{1}{\overline{m}_{\widetilde{l}_R}^2}\frac{(m_{\widetilde{l}_R}^2)_e^\mu}{\overline{m}_{\widetilde{l}_R}^2}\frac{M_1\mu\tan\beta}{\overline{m}_{\widetilde{l}_R}^2}f_1\left(\frac{\mu^2}{\overline{m}_{\widetilde{l}_R}^2}\right). \tag{2.15}$$

In the above equations, $\overline{m}_{\widetilde{l}_R}^2$ ($\overline{m}_{\widetilde{l}_L}^2$) stands for an averaged right-handed (left-handed) slepton mass, and $(m_{\widetilde{l}_R}^2)_e^\mu$ is a (μ, e) component of the right-handed charged slepton mass squared matrix. The kinematic function f_1 is given by

$$f_1(x) = -\frac{8 - 11x + 4x^2 - x^3 + 2(2 + x)\log x}{2(1 - x)^4} \tag{2.16}$$

which is a positive-definite, decreasing function of x.

A key point is that the relative sign of the two amplitudes is negative and then cancellation between diagrams can occur significantly. For $A_\mu = 0$, a severe cancellation happens when

$$\frac{1}{2\overline{m}_{\widetilde{l}_L}^2} - \frac{1}{\overline{m}_{\widetilde{l}_R}^2}f_1\left(\frac{\mu^2}{\overline{m}_{\widetilde{l}_R}^2}\right) \sim 0. \tag{2.17}$$

This cancellation occurs when $\overline{m}^2_{\tilde{l}_L} \sim \mu^2$ in the limit of $\mu^2/\overline{m}^2_{\tilde{l}_R} \gg 1$. Since dominant contributions for $\mu \to e\gamma$ and a^{SUSY}_μ are now different, then their correlation becomes much weaker than in the case that the left-handed sleptons have LFV masses.

Next, we consider the processes $\mu \to eee$ and $\mu \to e$ conversion in the nuclei. Their formulae are also given in [27]. See also ref. [40] for precise evaluation of $\mu \to e$ conversion in the nuclei. These two observables also suffer from the partial cancellation [39]. The $\mu \to eee$ receives dominant contribution from the penguin-type diagrams which are enhanced at large $\tan\beta$ region in a similar manner to $\mu \to e\gamma$ so that their behaviors are alike; the subdominant box-type contribution just helps lifting up the depth of the cancellation valley. On the other hand, the $\mu \to e$ conversion rate behaves rather differently and plays a complementary role in resolving the cancellation point. Thus, the correlation among the LFV processes are also weaker than the case that the left-handed sleptons have LFV masses.

3 Monte Carlo study

In this section, we study the leptonic SUSY signals at the LHC in the non-universal Higgs mass scenario. For our analysis, we use ISAJET v7.75 [41] to calculate the sparticle spectrum and IsaReD [42], which is part of the IsaTools package, to evaluate the dark matter relic density. We generated 5×10^6 events by HERWIG 6.5 [43]; this corresponds to about 300 fb^{-1} of integrated luminosity. The AcerDet package [44] is employed to simulate the detector response.

3.1 Model point

As mentioned earlier, we chose $m_{H_D} = m_0 \neq m_{H_U}$ at the GUT scale. We are interested in the case that both left- and right-handed sleptons can be directly produced via neutralino and chargino cascade decays. Then slepton masses should be light and a relatively small value of m_0 had been chosen. Furthermore, we chose a moderate value for $m_{1/2}$. The relevant parameters and sparticle masses for our studied point A are listed in table 1. We took $m_0 = 100\,\text{GeV}, m_{1/2} = 300\,\text{GeV}, m_{H_U} = 380\,\text{GeV}$. This leads to $\mu = 271\,\text{GeV}, m_{\tilde{e}_L} = 240\,\text{GeV}$, and $m_{\tilde{e}_R} = 130\,\text{GeV}$. We will see that this corresponds to the point where strong cancellation among contributions to $Br(\mu \to e\gamma)$ occurs.

For this choice of parameters, the value of μ substantially reduces from $\mu = 397.30\,\text{GeV}$ for mSUGRA case with inputs: $m_0 = 100\,\text{GeV}, m_{1/2} = 300\,\text{GeV}$, and $\tan\beta = 10$. This increases the Higgsino components of the LSP as the mixing matrix elements $(N_{\widetilde{B}}, N_{\widetilde{W}}, N_{\widetilde{H}_D}, N_{\widetilde{H}_U}) = (-0.96, 0.09, 0.22, -0.11)$. The dark matter relic density is evaluated to be 0.1179 which is consistent with the combined results from WMAP and SDSS [2, 3], $\Omega_{\text{DM}}h^2 = 0.111^{+0.011}_{-0.015}$ (2σ).

The relevant sparticle decay branching ratios are compared with mSUGRA case in table 2. In mSUGRA scenario, $\tilde{\chi}^0_1$ is almost pure Bino, and $\tilde{\chi}^0_2$ and $\tilde{\chi}^\pm_1$ are Wino-like. Then $\tilde{q}_L$ decays substantially into $\tilde{\chi}^0_2$ and $\tilde{\chi}^\pm_1$. As the decay into $\tilde{e}_L$ is kinematically forbidden for this parameter choice, they essentially decay into left-handed component of $\tilde{\tau}_1$ with large branching and small Bino component of $\tilde{\chi}^0_2$ could decay into $\tilde{e}_R$ producing the well-known edge of dilepton invariant mass distribution [45]. On the other hand,

m_0	100	$m_{1/2}$	300	m_{H_D}	100	m_{H_U}	380
$\tan\beta$	10	μ	271.33	M_1	122.49	M_2	230.89
$m_{\tilde{g}}$	719.67						
$m_{\tilde{u}_L}$	665.19	$m_{\tilde{u}_R}$	648.85	$m_{\tilde{d}_L}$	670.29	$m_{\tilde{d}_R}$	642.47
$m_{\tilde{b}_1}$	600.91	$m_{\tilde{b}_2}$	638.72	$m_{\tilde{t}_1}$	462.35	$m_{\tilde{t}_2}$	655.20
$m_{\tilde{e}_L}$	239.62	$m_{\tilde{e}_R}$	130.38	$m_{\tilde{\tau}_1}$	128.07	$m_{\tilde{\tau}_2}$	238.89
$m_{\tilde{\nu}}$	224.37	$m_{\tilde{\nu}_\tau}$	222.16	$m_{\tilde{\chi}_1^+}$	196.30	$m_{\tilde{\chi}_2^+}$	321.62
$m_{\tilde{\chi}_1^0}$	114.70	$m_{\tilde{\chi}_2^0}$	197.82	$m_{\tilde{\chi}_3^0}$	278.87	$m_{\tilde{\chi}_4^0}$	323.23
m_h	111.22	m_{H^0}	350.05	m_A	347.31	m_{H+}	358.56

Table 1. Relevant parameters and sparticle masses in GeV for the parameter point A.

	A	mSUGRA		A	mSUGRA
$\tilde{u}_L \to \tilde{\chi}_2^0$	25.4	31.6	$\tilde{\chi}_4^0 \to \tilde{e}_L$	2.3	1.0
$\tilde{u}_L \to \tilde{\chi}_3^0$	0.2	0.1	$\tilde{\chi}_4^0 \to \tilde{e}_R$	0.7	0.3
$\tilde{u}_L \to \tilde{\chi}_4^0$	7.8	1.3	$\tilde{\chi}_2^0 \to \tilde{e}_R$	13.5	3.1
$\tilde{u}_L \to \tilde{\chi}_1^+$	53.2	64.4	$\tilde{\chi}_2^+ \to \tilde{\nu}_L$	7.4	2.1
$\tilde{u}_L \to \tilde{\chi}_2^+$	13.1	1.8	$\tilde{\chi}_1^+ \to \tilde{\tau}_1$	88.8	63.3
$\tilde{d}_L \to \tilde{\chi}_2^0$	21.8	30.7	$\tilde{\nu}_L \to \tilde{\chi}_1^+$	26.1	-
$\tilde{d}_L \to \tilde{\chi}_3^0$	0.4	0.1	$\tilde{e}_L \to \tilde{\chi}_2^0$	26.5	5.9
$\tilde{d}_L \to \tilde{\chi}_4^0$	9.7	1.8	$\tilde{e}_L \to \tilde{\chi}_1^0$	35.9	84.0
$\tilde{d}_L \to \tilde{\chi}_1^-$	42.1	60.4	$\tilde{e}_R \to \tilde{\chi}_1^0$	100	100
$\tilde{d}_L \to \tilde{\chi}_2^-$	23.1	4.8			

Table 2. Relevant branching ratios in % for our sample point A compared with mSUGRA point.

heavier inos are Higgsino-like and would not be produced at the LHC. This will then forbid $\tilde{e}_L$ to show up at the LHC also.

For point A, when μ is smaller, heavier inos have larger Wino components so that their productions in the left-handed squark decay become significant. table 2 shows that $Br(\tilde{q}_L \to \tilde{\chi}_4^0/\tilde{\chi}_2^+)$, along with $Br(\tilde{\chi}_4^0 \to \tilde{e}_L)$ and $Br(\tilde{\chi}_2^+ \to \tilde{\nu}_L)$, are enhanced considerably. On the contrary, the enhancement in $Br(\tilde{\chi}_2^0 \to \tilde{e}_R)$ well demonstrates the increase of Bino component in $\tilde{\chi}_2^0$. Summarily, with small $\mu \sim m_{1/2}$, a number of sparticles could show up through various decay patterns, eq. (2.1), at the LHC experiment. Note that $\tilde{\chi}_3^0$ is almost pure Higgsino and then is not produced neither at point A nor mSUGRA point.

3.2 Two-lepton channel

In analyzing SUSY signals at the LHC, we put an emphasis on lepton channels when lepton presumably means electron or muon. In this section, we focus on the celebrated dilepton invariant mass distribution and model independent constraints on the sparticle masses. The other signatures will be discussed in the next section. The dominant neutralino and chargino cascade decay processes which lead to OSSF lepton pair in the final states and the corresponding expected kinematics endpoints are listed in table 3

decay mode	$m_{jll}^{\max}$	$m_{jll}^{\min}$	$m_{jl}^{\max}$	$m_{jl}^{\min}$	$m_{ll}^{\max}$
(1) $\tilde{q}_L \to \tilde{\chi}_2^0 \to \tilde{e}_R \to \tilde{\chi}_1^0$	517.4	209.1	477.6	272.7	70.7
(2) $\tilde{q}_L \to \tilde{\chi}_2^+ \to \tilde{\nu}_L \to \tilde{\chi}_1^+$	461.2	202.8	417.2	253.8	111.6
(3) $\tilde{q}_L \to \tilde{\chi}_4^0 \to \tilde{e}_L \to \tilde{\chi}_2^0$	459.8	223.4	390.2	285.7	122.4
(4) $\tilde{q}_L \to \tilde{\chi}_4^0 \to \tilde{e}_R \to \tilde{\chi}_1^0$	550.3	217.1	532.0	249.6	140.6
(5) $\tilde{q}_L \to \tilde{\chi}_4^0 \to \tilde{e}_L \to \tilde{\chi}_1^0$	550.5	296.5	510.4	383.6	190.5

Table 3. Endpoints of invariant mass distributions in GeV for various decay processes.
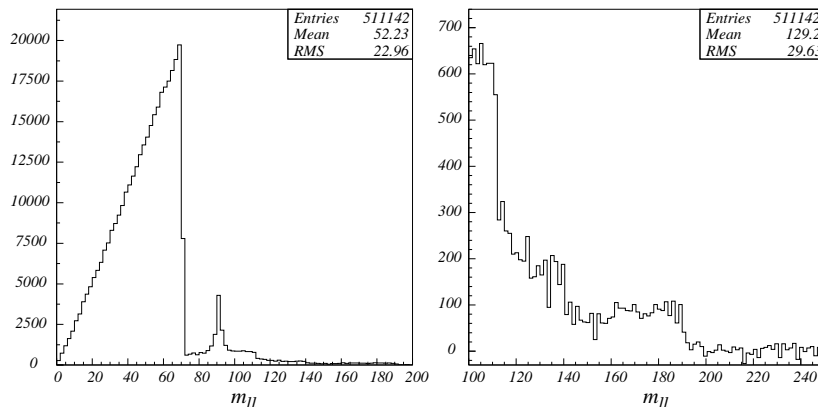
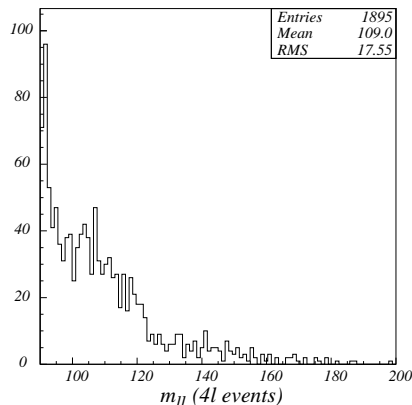**Figure 1**. Dilepton invariant mass distribution (in GeV).

The events are selected by the following criteria [46]:

- an OSSF dilepton pair where both leptons have $p_T^l > 10\,\text{GeV}$ and $|\eta| < 2.5$,

- more than 4 jets with $p_{T,1}^j > 100\,\text{GeV}, p_{T,2,3,4}^j > 50\,\text{GeV}$,

- $M_{\text{eff}} \equiv p_{T,1} + p_{T,2} + p_{T,3} + p_{T,4} + \not{E}_T > 400\,\text{GeV}$,

- $\not{E}_T > \max(100, 0.2 M_{\text{eff}})$.

The dilepton invariant mass distributions are shown in figure 1. In these plots, the subtraction of opposite sign opposite flavor (OSOF) dilepton distribution is utilized to reduce SUSY backgrounds. The endpoint position from $\tilde{q}_L \to \tilde{\chi}_i \to \tilde{l} \to \tilde{\chi}_j$ is given by analytical formula [45]

$$m_{ll}^{\max} = \sqrt{\frac{(m_{\tilde{\chi}_i}^2 - m_{\tilde{l}}^2)(m_{\tilde{l}}^2 - m_{\tilde{\chi}_j}^2)}{m_{\tilde{l}}^2}} \tag{3.1}$$

From the dilepton invariant mass distribution, edges of all decay modes except (3) in table 3 are visible. The distribution of decay mode (3) is small because basically $\tilde{\chi}_2^0$ decays further through the golden mode (1) and results in four-lepton final states discussed below.

Figure 2. Dilepton invariant mass m_{ll} distribution (in GeV) from four-lepton events with the requirement on the other lepton pair $m_{l'l'} < 70.7\,\mathrm{GeV}$.

3.3 Four-lepton channel

Thus, we turn to consider four-lepton events. If these leptons really come from the cascade decay

$$\tilde{\chi}_4^0 \to \tilde{e}_L \to \tilde{\chi}_2^0 \to \tilde{e}_R \to \tilde{\chi}_1^0, \tag{3.2}$$

they must form two OSSF pairs, and an invariant mass of one pair must be below the endpoint of mode (1) while another be lower than that of mode (3). This mode is very useful in the two senses. Basically, $m_{\tilde{\chi}_2^+} \sim m_{\tilde{\chi}_4^0}$, $m_{\tilde{\chi}_1^+} \sim m_{\tilde{\chi}_2^0}$ and $m_{\tilde{\nu}} \sim m_{\tilde{e}_L}$ so that the endpoints from modes (2) and (3) are close. If endpoints of other modes are much different from these two, by looking at $m_{ll(3)}^{\max}$ from four-lepton events, one can easily pinpoint which edge from dilepton events is the edge of mode (2). Moreover, we can use $m_{ll(3)}^{\max}$ as a cross check for $m_{\tilde{\chi}_4^0}$ and $m_{\tilde{e}_L}$ obtained from edges of mode (4) and (5).

We now consider the possibility to identify the decay mode (3) whose daughter $\tilde{\chi}_2^0$ subsequently decays via mode (1) producing four leptons in the final states. The following cuts are applied to select events:

- exactly two pairs of OSSF leptons where each lepton has $p_T^l > 10\,\mathrm{GeV}$ and $|\eta| < 2.5$,

- four leptons must be composed of exactly one e^+e^- pair and one $\mu^+\mu^-$ pair.

The m_{ee} and $m_{\mu\mu}$ are then calculated for each events. After requiring that an invariant mass of one OSSF lepton pair must less than $70.7\,\mathrm{GeV}$, distribution of the other pair is shown in figure 2. Now the edge around 122 GeV shows up confirming that events are truly from the decay in eq. (3.2). For a consistency check, we also plotted the trilepton and four-lepton invariant mass distributions from events which pass the above cuts; the plots are shown in appendix A. The fitted values of various endpoints are obtained by using linear fit function

$$f(M) = \begin{cases} AM + B, & 0 \le M \le M_{ll}^{\max} \\ 0, & M > M_{ll}^{\max} \end{cases} \tag{3.3}$$

smeared with a Gaussian and are listed in table 4.

Distribution	Expected endpoint	Fitted endpoint
$m_{ll(1)}$	70.78	70.67 ± 0.01
$m_{ll(2)}$	111.61	111.70 ± 0.21
$m_{ll(3)}$	122.41	121.93 ± 0.43
$m_{ll(4)}$	140.62	140.64 ± 0.26
$m_{ll(5)}$	190.46	191.05 ± 0.28

Table 4. Fitted endpoints in GeV

	$m_{\tilde{\chi}_1^0}$	$m_{\tilde{l}_R}$	$m_{\tilde{\chi}_2^0}$	$m_{\tilde{q}_L}$
Solution 1	114.70	130.38	197.82	665.19
Solution 2	178.09	244.03	265.06	747.22

Table 5. Sparticle mass ambiguities in GeV

3.4 Mass parameter determination

Once kinematical endpoints have been measured experimentally, relevant sparticle masses may be extracted. It is expected that $m_{\tilde{q}_L}, m_{\tilde{\chi}_2^0}, m_{\tilde{l}_R}$, and $m_{\tilde{\chi}_1^0}$ can be reconstructed from $m_{ll}^{\max}, m_{jll}^{\max}, m_{jl}^{\max}$ and $m_{jl}^{\min}$ [47]. Furthermore, if higher endpoints are visible, one would then be able to identify the decay of heavier neutralino and then resolve masses of $\tilde{\chi}_4^0$ and $\tilde{l}_L$.

For a given set of $m_{ll}^{\max}, m_{jll}^{\max}, m_{jl}^{\max}$ and $m_{jl}^{\min}$ measurements, in principle, there may be different corresponding sets of sparticle masses [48]. For the set of endpoints (1) in table 3, there are two possible solutions as listed in table 5. The second solution can be discarded by measuring $m_{jll}^{\min}$, which differs by around 20 GeV. Alternatively, solution 2 does not have solution for $m_{\tilde{e}_L}$ which satisfies $m_{ll(4)}^{\max}$ and $m_{ll(5)}^{\max}$ simultaneously.

In order to estimate error for each SUSY particle mass, we generated a set of random numbers corresponding to a set of masses $\{m_{\tilde{\chi}_1^0}, m_{\tilde{\chi}_2^0}, m_{\tilde{\chi}_4^0}, m_{\tilde{q}_L}, m_{\tilde{e}_L}\}$. We then calculated a set of measurable quantities $\{m_{jll}^{\min}, m_{jll}^{\max}, m_{jl}^{\min}, m_{jl}^{\max}, m_{ll(3,4,5)}^{\max}\}$ and their chi-squared which is defined as

$$\Delta\chi^2 = \sum_{\text{all observables}} \frac{(\text{Nominal value} - \text{Measured value})_i^2}{\sigma_i^2}. \tag{3.4}$$

In the above definition, σ_i includes both systematical error and statistical error. We employed systematical errors as listed in table 6 [49]. In our analysis, however, we used only statistical errors for $m_{ll(3,4,5)}^{\max}$ since they dominate over systematical errors (see table 4). Moreover, we fitted endpoints for $m_{jll}^{\min}, m_{jll}^{\max}, m_{jl}^{\min}, m_{jl}^{\max}$ distributions and found that even if they have good statistics, their fitted values curiously differ from central values, especially $m_{jll}^{\max}$. We then just used their systematical errors in calculating $\Delta\chi^2$.

In addition, the negligibly smallness of both systematical and statistical errors for $m_{ll(1)}^{\max}$ implies that $m_{\tilde{e}_R}$ will be measured rather precisely. Therefore, in the analysis, we took $m_{ll(1)}^{\max}$ as an input and obtained $m_{\tilde{e}_R}$ for given values of $\{m_{\tilde{\chi}_1^0}, m_{\tilde{\chi}_2^0}\}$. Results of 1-$\sigma$ error estimation for sparticle mass differences are shown in table 7.

Distribution	Systematical error (GeV)
$m_{ll}^{\max}$	0.08
$m_{jll}^{\max}$	4.3
$m_{jll}^{\min}$	2.0
$m_{jl}^{\max}$	3.8
$m_{jl}^{\min}$	3.0

Table 6. Estimated systematical errors for different endpoints (in GeV).

Sparticle Mass	Central value	Estimated error
$m_{\tilde{\chi}_1^0}$	114.70	$^{+6.7}_{-6.3}$
$m_{\tilde{e}_R} - m_{\tilde{\chi}_1^0}$	15.68	$^{+0.45}_{-0.49}$
$m_{\tilde{\chi}_2^0} - m_{\tilde{\chi}_1^0}$	83.12	$^{+0.75}_{-0.62}$
$m_{\tilde{e}_L} - m_{\tilde{\chi}_1^0}$	124.92	$^{+0.65}_{-0.65}$
$m_{\tilde{\chi}_4^0} - m_{\tilde{\chi}_1^0}$	208.53	$^{+0.77}_{-0.64}$
$m_{\tilde{q}_L} - m_{\tilde{\chi}_1^0}$	551.19	$^{+4.64}_{-4.47}$

Table 7. Central values and 1-σ error estimation of relevant sparticle masses in GeV.

4 Flipping solutions

Besides the one shown in table 5, there is another kind of ambiguities which is related to parameter point identification especially when the ordering of μ, M_1 and M_2 is shuffled. We now introduce flipping solutions. Flipping solutions are solutions among which masses of relevant sparticles (masses of left-handed squark, left- and right-handed sleptons, and three neutralinos which have significant gaugino component) are the same but ordering of M_1, M_2 and μ parameters are different. The mass degeneracy among solutions results in the same endpoint positions from those sparticle decay. Therefore, only endpoint measurement is not enough to distinguish these solutions. By reminding that $M_1 < M_2 < \mu$ for point A, we illustrate another two flipping solutions: $M_1 < \mu < M_2$ (point A2) and $\mu < M_1 < M_2$ (point A3); their relevant parameters are listed in table 8.

We fixed three masses of neutralinos which have significant gaugino component equal, as they are frequently produced from squark decays and would be measured rather precisely. For points A and A2, such three neutralino states are $\tilde{\chi}_1^0, \tilde{\chi}_2^0$ and $\tilde{\chi}_4^0$, so almost all masses except $m_{\tilde{\chi}_3^0}$ for both points are degenerate ($m_{\tilde{\chi}_3^0}|_{\text{pointA}} = 279\,\text{GeV}$ and $m_{\tilde{\chi}_3^0}|_{\text{pointA2}} = 234\,\text{GeV}$). For point A3, however, they are $\tilde{\chi}_1^0, \tilde{\chi}_3^0$ and $\tilde{\chi}_4^0$ instead. Therefore, we fixed $m_{\tilde{\chi}_3^0} = m_{\tilde{\chi}_2^0}|_{\text{pointA}}$ and $m_{\tilde{\chi}_2^0} = 155\,\text{GeV}$. On the other hand, $\tilde{\chi}_3^0$ for points A and A2 and $\tilde{\chi}_2^0$ for point A3 are nearly pure Higgsino, and they are not produced from squark decays, so that the experimental constraint would be weaker.

In the followings, we discuss and compare some phenomenological signatures of all flipping solutions. We will show that different properties of neutralinos essentially lead to discrepancy in both collider and low-energy LFV observables.

	A	A2	A3		A	A2	A3
μ	271.33	226.06	146.21				
M_1	122.49	125.66	187.46	M_2	230.89	272.86	291.47
$m_{\tilde{u}_L}$	665.19	665.19	665.19	$m_{\tilde{u}_R}$	648.85	649.84	657.09
$m_{\tilde{d}_L}$	670.29	670.29	670.29	$m_{\tilde{d}_R}$	642.47	641.67	643.68
$m_{\tilde{e}_L}$	239.62	239.62	239.62	$m_{\tilde{e}_R}$	130.38	130.38	130.38
$m_{\tilde{\tau}_2}$	238.89	270.32	292.60	$m_{\tilde{\tau}_1}$	128.07	123.82	173.80
$m_{\tilde{\nu}}$	224.37	224.03	223.92	$m_{\tilde{g}}$	719.67	719.35	720.81
$m_{\tilde{\chi}_1^+}$	196.30	193.34	133.27	$m_{\tilde{\chi}_2^+}$	321.62	320.88	319.79
$m_{\tilde{\chi}_1^0}$	114.70	114.70	114.70	$m_{\tilde{\chi}_2^0}$	197.82	197.82	155.17
$m_{\tilde{\chi}_3^0}$	278.87	234.28	197.82	$m_{\tilde{\chi}_4^0}$	323.23	323.23	323.23

Table 8. Relevant parameters and sparticle masses in GeV for points A, A2 and A3 respectively.

	A	A2		A	A2		A	A2
$\tilde{u}_L \to \tilde{\chi}_2^0$	25.4	15.4	$\tilde{u}_R \to \tilde{\chi}_2^0$	4.1	9.6	$\tilde{\chi}_2^0 \to \tilde{e}_R$	13.5	14.1
$\tilde{u}_L \to \tilde{\chi}_4^0$	7.8	17.8	$\tilde{d}_R \to \tilde{\chi}_2^0$	4.1	9.6	$\tilde{\chi}_2^+ \to \tilde{\nu}_L$	7.4	12.9
$\tilde{u}_L \to \tilde{\chi}_2^+$	13.1	33.2	$\tilde{\chi}_4^0 \to Z + \tilde{\chi}_2^0$	0.2	0.2	$\tilde{\chi}_2^+ \to Z + \tilde{\chi}_1^+$	16.1	13.4
$\tilde{d}_L \to \tilde{\chi}_2^0$	21.8	10.4	$\tilde{\chi}_4^0 \to Z + \tilde{\chi}_1^0$	1.4	0.3	$\tilde{\nu}_L \to \tilde{\chi}_1^+$	26.1	20.4
$\tilde{d}_L \to \tilde{\chi}_4^0$	9.7	20.5	$\tilde{\chi}_4^0 \to \tilde{e}_L$	2.3	4.2	$\tilde{e}_L \to \tilde{\chi}_2^0$	26.5	25.6
$\tilde{d}_L \to \tilde{\chi}_2^-$	23.1	45.2	$\tilde{\chi}_4^0 \to \tilde{e}_R$	0.7	0.3	$\tilde{e}_L \to \tilde{\chi}_1^0$	35.9	47.8

Table 9. Comparison between relevant branching ratios in % for points A and A2.

4.1 Branching ratios

First of all, we show the OSSF dilepton distributions in figure 3. The total number of generated events is 5×10^6 for all points. This corresponds to about 300 fb^{-1} for points A and A2 and 250 fb^{-1} for point A3. The difference between distribution for points A and A2 is conspicuous. Since $\tilde{\chi}_2^\pm$ and $\tilde{\chi}_4^0$ are Wino-like at point A2, $Br(\tilde{q}_L \to \tilde{\chi}_2^+/\tilde{\chi}_4^0)$ and $Br(\tilde{\chi}_2^+/\tilde{\chi}_4^0 \to \tilde{l}_L/\tilde{\nu}_L)$ are enhanced (see table 9). These result in the Z peak and the height of edges around 110 GeV (from $\tilde{\chi}_2^+ \to \tilde{\nu}_L \to \tilde{\chi}_1^+$) and 190 GeV (from $\tilde{\chi}_4^0 \to \tilde{e}_L \to \tilde{\chi}_1^0$) for A2 at least twice the size of that for point A.

The enhancement of the branching ratios $Br(\tilde{q}_L \to \tilde{\chi}_2^+)$ and $Br(\tilde{\chi}_2^+ \to \tilde{\nu}_L)$ can be understood analytically. Consider the $\tilde{\chi}_2^\pm$-lepton-slepton interaction
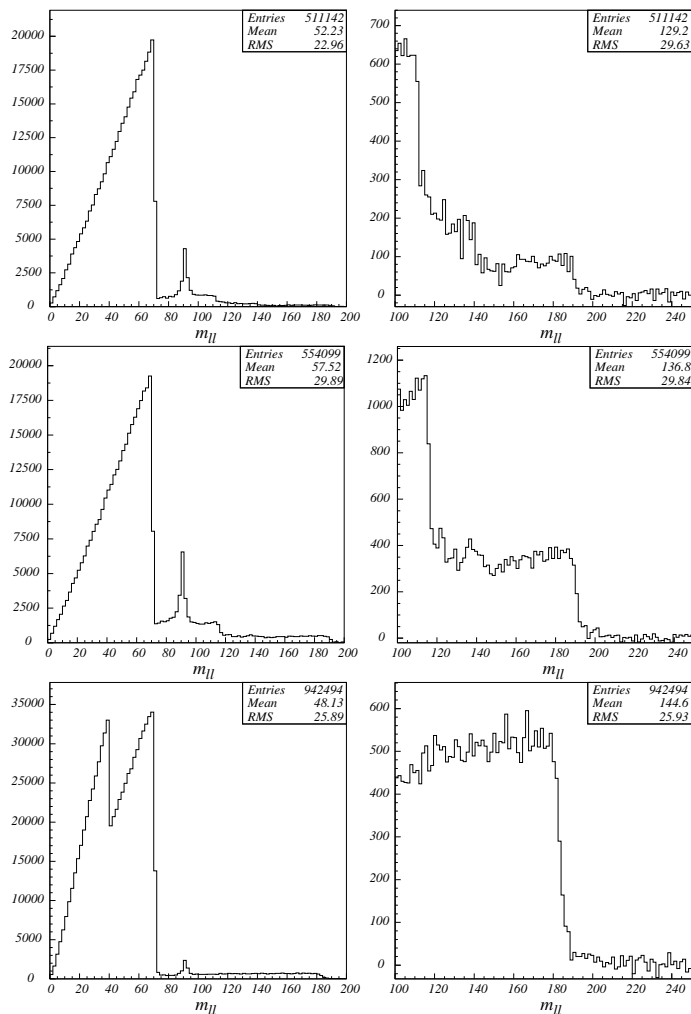
$$\mathcal{L} \propto g \sin \phi_R (\tilde{\nu}^* \overline{\tilde{\chi}}_2^- P_L e + \bar{e} P_R \tilde{\chi}_2^- \tilde{\nu}) + g \sin \phi_L (\tilde{e}_L^* \overline{\tilde{\chi}}_2^+ P_L \nu + \bar{\nu} P_R \tilde{\chi}_2^+ \tilde{e}_L). \tag{4.1}$$

Here $P_{L,R}$ stands for left-, right-handed projection operator and the mixing angles ϕ_L and ϕ_R are given (with two-fold ambiguity) by

$$\tan 2\phi_L = \frac{2\sqrt{2}m_W(M_2 \cos \beta + \mu \sin \beta)}{M_2^2 - \mu^2 - 2m_W^2 \cos 2\beta}, \tag{4.2}$$

$$\tan 2\phi_R = \frac{2\sqrt{2}m_W(M_2 \sin \beta + \mu \cos \beta)}{M_2^2 - \mu^2 + 2m_W^2 \cos 2\beta}. \tag{4.3}$$

Figure 3. OSSF dilepton invariant mass distribution for points A, A2 and A3 respectively. Right panels show a close-up of higher endpoints.

The interaction $\widetilde{\chi}_2 - \tilde{\nu} - e$ and, analogously, $\widetilde{\chi}_2 - \tilde{u} - d$ are proportional to $\sin\phi_R$ which becomes larger when M_2 and μ are inverted so that $\mu < M_2$, for moderate $\tan\beta$.

Point A3 can also be distinguished from the others. The important key is that, for point A3, mass difference $m_{\tilde{\chi}_2^+} - m_{\tilde{\chi}_1^+}$ is close to $m_{\tilde{\chi}_4^0} - m_{\tilde{\chi}_1^0}$, in addition to $m_{\tilde{\chi}_4^0} - m_{\tilde{\chi}_2^0}$. Hence the dislocation of $m_{ll}^{\max}(\tilde{\chi}_2^+ \to \tilde{\nu}_L \to \tilde{\chi}_1^+)$ will serve as an indicator of flipping solution. In figure 3, the highest endpoint around 180 GeV for point A3 actually comes from the decay $\tilde{\chi}_2^+ \to \tilde{\nu}_L \to \tilde{\chi}_1^+$, while the distribution for $\tilde{\chi}_4^0 \to \tilde{e}_L \to \tilde{\chi}_1^0$ ($m_{ll}^{\max} \sim 190$ GeV) is much smaller.

In addition, the study of four-lepton events in analogous to subsection 3.3 reveals the endpoint from the decay chain $\tilde{\chi}_4^0 \to \tilde{e}_L \to \tilde{\chi}_3^0$ ($m_{ll}^{\max} \sim 120$ GeV) where $\tilde{\chi}_3^0$ subsequently undergoes the cascade decay $\tilde{\chi}_3^0 \to \tilde{e}_R \to \tilde{\chi}_1^0$. By utilizing all endpoint information from four-lepton events, $\tilde{\chi}_4^0$ and $\tilde{e}_L$ masses can be extracted and $m_{ll}^{\max}(\tilde{\chi}_4^0 \to \tilde{e}_L \to \tilde{\chi}_1^0) \sim 190$ GeV can be calculated. To this end, one can confirm that the m_{ll} endpoint at 180 GeV

Point A4:

μ	205.64	M_1	253.75	M_2	414.91		
$m_{\tilde{u}_L}$	747.54	$m_{\tilde{u}_R}$	696.83	$m_{\tilde{d}_L}$	752.02	$m_{\tilde{d}_R}$	680.72
$m_{\tilde{e}_L}$	389.37	$m_{\tilde{e}_R}$	243.92	$m_{\tilde{\tau}_2}$	387.60	$m_{\tilde{\tau}_1}$	233.51
$m_{\tilde{\nu}}$	380.13	$m_{\tilde{g}}$	766.77	$m_{\tilde{\chi}_1^+}$	198.64	$m_{\tilde{\chi}_2^+}$	435.96
$m_{\tilde{\chi}_1^0}$	179.04	$m_{\tilde{\chi}_2^0}$	212.99	$m_{\tilde{\chi}_3^0}$	265.21	$m_{\tilde{\chi}_4^0}$	440.05

Table 10. Relevant parameters and sparticle masses in GeV for point A4.
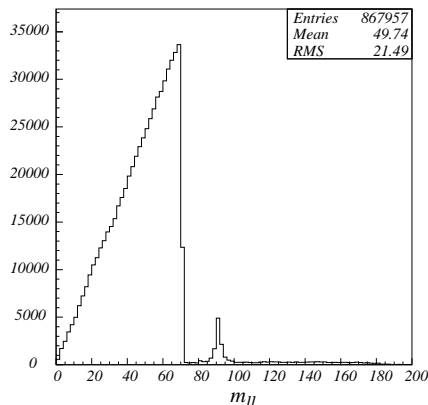
Figure 4. OSSF dilepton invariant mass distribution for point A4.

does not come from $\tilde{\chi}_4^0$ decay.

A very striking feature of its double peak distribution below the Z peak in figure 3 seems to make $\mu < M_1 < M_2$ case very easily distinguishable from other cases. However, this actually depends on our model parameter choice, i.e. $m_{\tilde{e}_R} - m_{\tilde{\chi}_1^0} \ll m_{\tilde{\chi}_2^0} - m_{\tilde{e}_R}$. The distribution receives contribution to the outer edge (around $70\,\text{GeV}$) from the Bino-like $\tilde{\chi}_3^0$ cascade decay $\tilde{\chi}_3^0 \to \tilde{l}_R \to \tilde{\chi}_1^0$ and to the inner edge (around $40\,\text{GeV}$) from the Higgsino-Bino mixed $\tilde{\chi}_2^0$ cascade decay $\tilde{\chi}_2^0 \to \tilde{l}_R \to \tilde{\chi}_1^0$. Consider the case that our true model point is the solution 2 in table 5. Its $\mu < M_1 < M_2$ flipping solution (point A4) has $m_{\tilde{\chi}_2^0} < m_{\tilde{e}_R}$ and an unusual double peak distribution disappears. We show mass spectrum of the point in table 10 and m_{ll} distribution in figure 4.

4.2 2 jets + $\not{E}_T$ signature

The distinctive Higgsino-like property of $\tilde{\chi}_1^0$ for very small μ solution makes it possible to distinguish one from intermediate-to-large μ solutions. More specifically, it is clearly presented in the differences in the decay branching ratio

$$Br(\tilde{q}_R \to \tilde{\chi}_1^0) = \begin{cases} 0.94 & \text{point A} \\ 0.89 & \text{point A2} \\ 0.16 & \text{point A3} \end{cases} .$$

When both pair-produced right-handed squarks decay directly into $\tilde{\chi}_1^0$, their signature is two high p_T jets + large $\not{E}_T$ and no isolated lepton in the final states. Here, we first
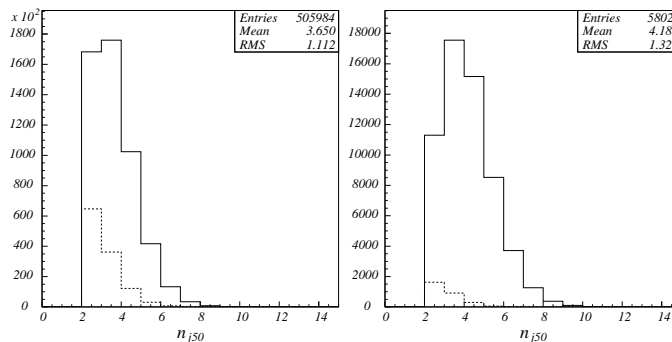
Figure 5. The number distributions of jet with $p_T > 50$GeV after the event cuts for point A and A3, respectively. The dashed line represents the distribution for $pp \to \tilde{q}_R \tilde{q}_R \to \tilde{\chi}_1^0 \tilde{\chi}_1^0$. Notice that the vertical axis of the left-handed figure is multiplied by 100.

count number of jets. We select events by employing the following cuts:

(c1) more than 2 jets with $|\eta_i| < 2.5$ and transverse momentum $p_{T,1} > 250\,\text{GeV}, p_{T,2} > 200\,\text{GeV}$,

(c2) no isolated lepton with p_T greater than $10\,\text{GeV}$,

(c3) no tagged b-jet,

(c4) $\not{E}_T > 250\,\text{GeV}$.

The number distribution of jet with $p_T > 50\,\text{GeV}$, n_{j50}, after cuts is shown in figure 5. Note that the distribution for point A2 is very similar to that for point A and therefore not shown here. There are obviously two differences between these two plots. Firstly, high jet-p_T cut (c1) and lepton cut (c2) reduce the number of events for point A3 so substantially that it is an order of magnitude smaller. Secondly, point A3 has smaller fraction of events for $n_{j50} = 2$ and larger fraction when $n_{j50} > 4$. These all indicate that squark tends to decay via a longer cascade decay which produces leptons or several softer jets in the final states. It further implies that squarks would have considerable decay branching ratio into heavier inos and the LSP has small gaugino components, i.e. Higgsino-like. To this end, one can infer that point A3 has small $\mu < M_1, M_2$.

In the same plots, the dashed line represents distribution of $pp \to \tilde{q}_R \tilde{q}_R \to \tilde{\chi}_1^0 \tilde{\chi}_1^0$ events. Even though there must have only two jets at parton level, the initial state radiation can contribute to the high p_T third and forth jets. The difference between the solid and dashed line receives contributions mostly from left-handed squark or gluino (associated) production.

The method of counting jet numbers, however, is not so reliable. We need more concrete evidence to confirm the conclusions about small $Br(\tilde{q} \to \tilde{\chi}_1^0)$ and hence small value of μ. This can be achieved by the so-called m_{T2} method [52]. The m_{T2} variable is defined in event-by-event basis as

$$m_{T2}(\mathbf{p}_T^{j_1}, \mathbf{p}_T^{j_2}, \not{p}_T^{\text{miss}}; m_{\text{test}}) \equiv \min_{\not{p}_T^\alpha + \not{p}_T^\beta = \not{p}_T^{\text{miss}}} \left[\max \left\{ m_T(\mathbf{p}_T^{j_1}, \not{p}_T^\alpha; m_{\text{test}}), m_T(\mathbf{p}_T^{j_2}, \not{p}_T^\beta; m_{\text{test}}) \right\} \right] \quad (4.4)$$
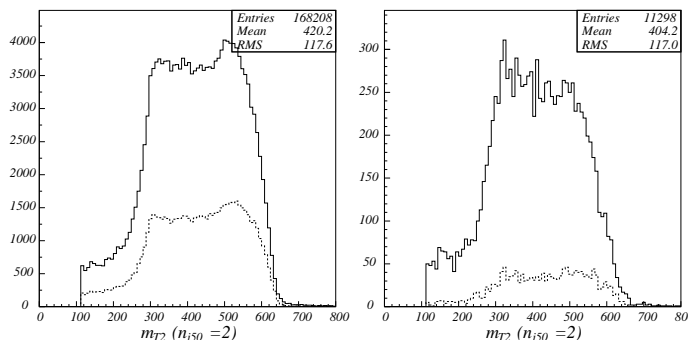
Figure 6. m_{T2} distribution for $n_{j50} = 2$. The left and right panels are for point A and A3 respectively. The dashed line represents the distribution for $pp \to \tilde{q}_R \tilde{q}_R \to \tilde{\chi}_1^0 \tilde{\chi}_1^0$.

where m_{test} is a test mass and the minimization is performed over all possible splitting $\not{p}_T^\alpha + \not{p}_T^\beta = \not{p}_T^{\text{miss}}$. The transverse mass m_T is defined as

$$m_T^2(\mathbf{p}_T^j, \not{p}_T^\alpha; m_{\text{test}}) \equiv m_j^2 + m_{\text{test}}^2 + 2\left(E_T^j \not{E}_T^\alpha - \mathbf{p}_T^j \cdot \not{p}_T^\alpha\right). \tag{4.5}$$

The m_{T2} variable has the property

$$m_{T2}(m_{\text{test}} = m_{\tilde{\chi}_1^0}) \leq m_{\tilde{q}_R}, \tag{4.6}$$

for $pp \to \tilde{q}_R \tilde{q}_R \to \tilde{\chi}_1^0 \tilde{\chi}_1^0$ events, so that one can determine $m_{\tilde{q}_R}$ from the endpoint measurement of m_{T2} distribution.

Figure 6 shows m_{T2} distributions for $n_{j50} = 2$. Here, m_{test} is taken to be the nominal value of $m_{\tilde{\chi}_1^0}$. Clearly, both m_{T2} distributions with $n_{j50} = 2$ have endpoint about the correct $\tilde{q}_R$ masses. However, the distribution for point A has sharp edge and events near the edge come mostly from the true cascade while that for A3 is contaminated mostly by contribution from $\tilde{q}_L$ production.

In order to estimate a statistical significance of signal over SM background, we adopted a set of event selection cuts from [53]:

- $\not{E}_T > \max(200\,\text{GeV}, 0.25 M_{\text{eff}})$ and $M_{\text{eff}} > 500\,\text{GeV}$,

- two jets with $p_T > \max(200\,\text{GeV}, 0.25 M_{\text{eff}}), |\eta| < 1$ and $\Delta R > 1$,

- no additional jet with $p_T > \min(200\,\text{GeV}, 0.15 M_{\text{eff}})$,

- no isolated leptons and no tagged b-jets,

- transverse sphericity $S_T > 0.2$.

It should be noted here that the above two hardest p_T jet cut, $p_T > \max(200\,\text{GeV}, 0.25 M_{\text{eff}})$, distorts shape of m_{T2} distribution. This is because the event near m_{T2} endpoint corresponds to the configuration where two jets go in the same direction with $p_{T,j} \sim 0.25 M_{\text{eff}}$. Therefore, this cut kills significant numbers of events near the endpoint.
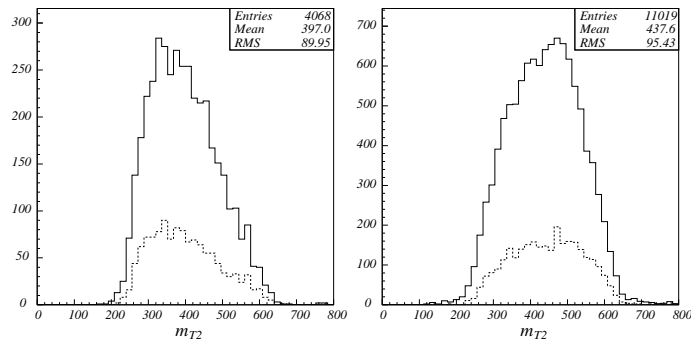
Figure 7. m_{T2} distribution of point A at $30\,fb^{-1}$ of integrated luminosity. In the left panel, selection cuts are taken from [53]. The two hardest p_T jet cut is different for the right panel as described in the text. Again, the dashed line represents the distribution for $pp \to \tilde{q}_R\tilde{q}_R \to \tilde{\chi}_1^0\tilde{\chi}_1^0$.

Point	No. of Signal	No. of SM Background	S/B_{SM}	$S/\sqrt{B_{SM}}$
A	1341	180	7.5	100.0
A3	133	180	0.7	9.9

Table 11. The number of signal and SM background events passing the selection cuts described in the text, signal-to-SM background ratio, and signal statistical significance for points A and A3 at $10\,fb^{-1}$ of integrated luminosity.

In figure 7, we just show how m_{T2} distribution is distorted. On the left panel, m_{T2} distribution for point A is shown when the above cuts are applied at $\sim 30\,fb^{-1}$ of integrated luminosity. It is an M_{eff} dependence of the cut that selects events with rather high p_T jets. If this cut is relaxed to be $p_{T,1} > 250\,\text{GeV}, p_{T,2} > 200\,\text{GeV}$, in the right panel, the peak of m_{T2} distribution leans more toward its edge as it is supposed to be. Moreover, the number of events passing the cuts are about three times larger with increasing fraction of $pp \to \tilde{q}_R\tilde{q}_R \to \tilde{\chi}_1^0\tilde{\chi}_1^0$ events near endpoint.

The signal-to-background ratio and signal statistical significance of events passing above cuts for $10\,fb^{-1}$ of integrated luminosity are given in table 11 for points A and A3. The background statistics is taken from [53], page 1630. The signal statistic of point A3 is so poor that its m_{T2} distribution is submerged in SM background. This makes it even easier to distinguish between two points.

Summarily, by investigating the m_{T2} distribution and branching ratio of heavier ino decay, the region to which the μ parameter belongs can be ascertained.

4.3 Charge asymmetry

In this subsection, we will illustrate that a charge asymmetry between the jl^+ and jl^- invariant mass distributions can help lift degeneracy between points A and A2. This method was firstly proposed in [50] where the decay $\tilde{q}_L \to \tilde{\chi}_2^0 \to \tilde{l}_\beta$ is studied in the case that slepton is purely right-handed; later the left-right mixing was taken into account in [51]. In our study, we assume that left-right slepton mixing is negligible. We now briefly explain the method following prescription in [50].

Consider the cascade decay $\tilde{q}_\alpha \to q\tilde{\chi}_i^0 \to q l_{\text{near}} \tilde{l}_\beta$ where l_{near} denotes lepton from $\tilde{\chi}_i^0$ decay and $\alpha, \beta = L, R$. The $q l_{\text{near}}$ invariant mass is given by a simple kinematics expression

$$(m_{q l_{\text{near}}})^2 = (m_{q l_{\text{near}}}^{\text{max}})^2 s_{\theta/2}^2 \tag{4.7}$$

where $s_{\theta/2} \equiv \sin(\theta/2)$ and θ is the angle between quark and lepton momenta in $\tilde{\chi}_i^0$ rest frame. Due to the chirality structure of quark-squark-neutralino coupling, $\tilde{\chi}_i^0$ is polarized. Its polarization alters the angular distribution of its daughter lepton and hence the angular distribution of $q l_{\text{near}}$ invariant mass. Mathematically, the probability density function receives extra angular-dependent factors from the chirality projector. For the case $\alpha \neq \beta$, the probability density is given by

$$\frac{dP}{ds_{\theta/2}} = \begin{cases} 4 s_{\theta/2}^3 & \text{for} \quad q l_{\text{near}}^+ \text{ or } \bar{q} l_{\text{near}}^- \\ 4 s_{\theta/2}(1 - s_{\theta/2}^2) & \text{for} \quad q l_{\text{near}}^- \text{ or } \bar{q} l_{\text{near}}^+ \end{cases} . \tag{4.8}$$

If $\alpha = \beta$, the density function for $q l_{\text{near}}^-$ and $\bar{q} l_{\text{near}}^+$ are inverted. Based on the fact that valence quarks have harder PDFs than sea quarks, squarks would be produced via $\tilde{q}\tilde{g}$ production more than anti-squarks. In the following, we therefore assume that high-p_T jet represents quark rather than anti-quark.

Define charge asymmetry

$$A \equiv \frac{s^+ - s^-}{s^+ + s^-} \qquad \text{where} \qquad s^\pm = \int_{(m_{q l^\pm}^{\text{max}})/2}^{m_{q l^\pm}^{\text{max}}} d\sigma(m_{q l^\pm}). \tag{4.9}$$

We obtain

$$A = \begin{cases} + & \text{for} \quad \alpha \neq \beta \\ - & \text{for} \quad \alpha = \beta \end{cases} . \tag{4.10}$$

For the celebrated decay mode $\tilde{q}_L \to \tilde{\chi}_2^0 \to \tilde{l}_R$, l_{near} with positive charge rather than negative charge favors to go to the opposite direction to the quark jet and constitutes events near endpoint. The charge asymmetry for this case is then positive.

In our study, once we know that the LSP is Bino-like by m_{T2} method and that $\tilde{q}_L$ cascades via long decay chains, this method can be used to probe the property of $\tilde{\chi}_2^0$. Figure 8 shows $N(j_h l^+) - N(j_h l^-)$ as a function of $m_{j_h l}$ for points A and A2 at $\sim 60\, fb^{-1}$ of integrated luminosity. In these plots, we use only j_h, one of the two highest p_T jets which gives higher m_{jll} value. Moreover, $m_{j_h l}$ is calculated only for lepton with higher p_T because $m_{\tilde{\chi}_2^0} - m_{\tilde{e}_R} > m_{\tilde{e}_R} - m_{\tilde{\chi}_1^0}$ and lepton from $\tilde{\chi}_2^0$ decays tends to have larger p_T. In addition, we require $m_{ll} < 70.7\, \text{GeV}$ and $m_{jll} < m_{jll}^{\text{max}}$. For point A (left), the charge asymmetry is clearly positive which indicates the $\tilde{q}_L \to \tilde{\chi}_2^0 \to \tilde{l}_R$ decay. On the right panel, the asymmetry is also positive but less prominent. At $m_{j_h l} > 300\, \text{GeV}$, the distribution is relatively flat compared to the left panel. This can be interpreted as the contribution from $\tilde{q}_R$ decay. The actual ratio of $Br(\tilde{q}_R \to \tilde{\chi}_2^0)/Br(\tilde{q}_L \to \tilde{\chi}_2^0)$ is

$$\frac{Br(\tilde{q}_R \to \tilde{\chi}_2^0)}{Br(\tilde{q}_L \to \tilde{\chi}_2^0)} = \begin{cases} 0.16 & \text{point A} \\ 0.67 & \text{point A2} \end{cases} .$$
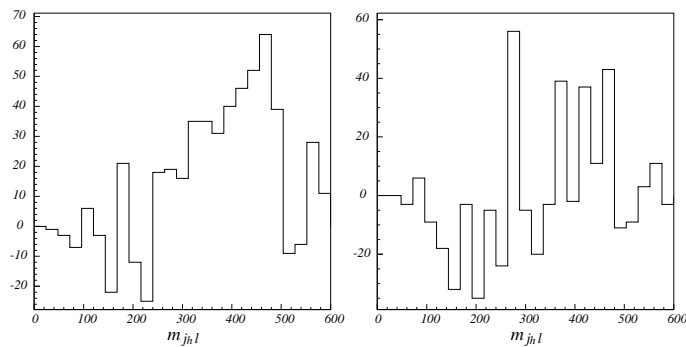
Figure 8. The difference between $m_{j_h l^+}$ and $m_{j_h l^-}$ distributions as a function of $m_{j_h l}$ for points A and A2.
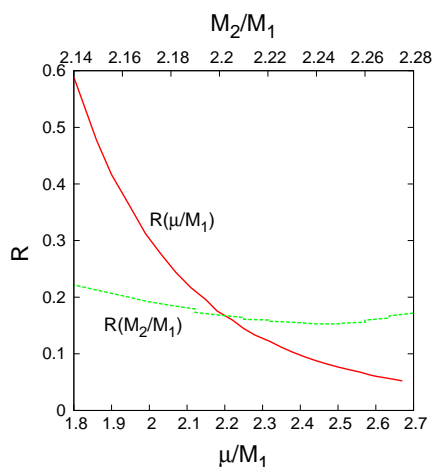
**Figure 9**. The ratio $Br(\tilde{u}_R \to \tilde{\chi}_2^0)/Br(\tilde{u}_L \to \tilde{\chi}_2^0)$

The ratios differ by factor of four: a factor two from the reduction of $Br(\tilde{q}_L \to \tilde{\chi}_2^0)$ and another from the enhancement of $Br(\tilde{q}_R \to \tilde{\chi}_2^0)$ (see table 9). This makes the contribution from $\tilde{q}_R$ for point A2 comparable to $\tilde{q}_L$'s contribution and really cause the decrease in the charge asymmetry. Therefore the flatness of charge asymmetry implies that $\tilde{\chi}_2^0$ have smaller Wino component and it is persuasive to conclude that $M_1 < \mu < M_2$ for this point.

In figure 9, we show the dependence of $R \equiv Br(\tilde{u}_R \to \tilde{\chi}_2^0)/Br(\tilde{u}_L \to \tilde{\chi}_2^0)$ on μ/M_1 and M_2/M_1. Here, we took parameter point A and allow μ and M_2 to deviate within 20 percent. The ratio R shows little dependence on M_2/M_1 while it ranges from below 0.1 to 0.6 when μ/M_1 ratio varies from 1.5 to 2.7. Due to the form of neutralino mass matrix, Wino mixes with Higgsinos easier than with Bino. Therefore, as a probe into the reduction of Wino component of $\tilde{\chi}_2^0$, the ratio R depends on μ/M_1 stronger than on M_2/M_1. When μ/M_1 is smaller, mixing between neutralino states is larger and the charge asymmetry receives more $\tilde{q}_R$ contribution so that the distribution becomes flat.

Now we give comments on other possible flipping solutions. The first possibility is a solution when $M_1 < M_2, \mu$ and $m_{\tilde{e}_R}$ and $m_{\tilde{e}_L}$ are flipped. This case can be easily distinguished by utilizing a charge asymmetry to confirm the chirality of a daughter slepton

Parameters	Resolving Methods
$\mu < M_1, M_2$	$m_{ll}^{\max}(\tilde{\chi}_2^+ \to \tilde{\nu}_L \to \tilde{\chi}_1^+) + m_{T2}$
$M_2 < M_1$	$m_{ll}^{\max}(\tilde{\chi}_2^+ \to \tilde{\nu}_L \to \tilde{\chi}_1^+)$
$M_1 < \mu < M_2$	branching ratio + charge asymmetry
$m_{\tilde{e}_L} \leftrightarrow m_{\tilde{e}_R}$	charge asymmetry

Table 12. Possible flipping solutions and resolving methods.
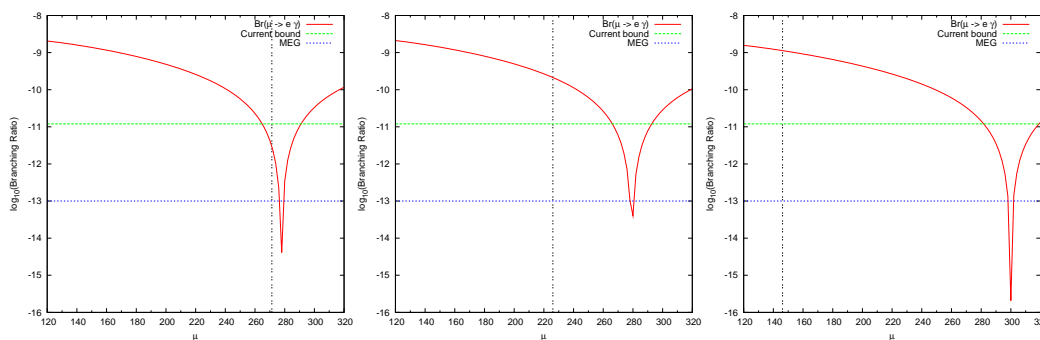
Figure 10. $Br(\mu \to e\gamma)$ as a function of μ for points A, A2 and A3 respectively. We assume the MSSM with horizontal symmetry given in section II. In these plots, $x = 0.30$ and a vertical line shows the nominal μ value for each point.

in the decay $\tilde{q}_L \to \tilde{\chi}_i^0 \to \tilde{l}_\beta$. However, if not only $m_{\tilde{e}_R}$ and $m_{\tilde{e}_L}$, but also $m_{\tilde{q}_R}$ and $m_{\tilde{q}_L}$, and M_1 and M_2 are inverted with $M_2 < M_1, \mu$, events near $m_{ll}^{\max} \sim 71\,\text{GeV}$ comes from $\tilde{q}_R \to \tilde{\chi}_2^0 \to \tilde{l}_L \to \tilde{\chi}_1^0$ instead and charge asymmetry of the original and this solutions must be the same. Nevertheless, whenever M_1 and M_2 are flipped, the chargino sector will be affected. For example, for $M_2 < M_1 < \mu$, mass splitting $m_{\tilde{\chi}_2^+} - m_{\tilde{\chi}_1^+}$ will be close to $m_{\tilde{\chi}_4^0} - m_{\tilde{\chi}_1^0}$ and hence endpoint position from $(\tilde{\chi}_2^+ \to \tilde{\nu}_L \to \tilde{\chi}_1^+)$ will generally differ from $m_{ll}^{\max} \sim 112\,\text{GeV}$.

We end this section by a table summarizing possible flipping solutions and methods to resolve it, table 12.

5 Implication to LFV processes

We begin this subsection by showing the dependence of $Br(\mu \to e\gamma)$ on μ parameter for three model points, together with current and future experimental bounds, in figure 10. In these plots, we took μ, M_1 and M_2 of our model points A, A2 and A3, and assumed flavor-violating parameters as the model with horizontal symmetry described in section II with $x = 0.30$. Here, we ignore the left-handed slepton mixings since we are interested in the cancellation among diagrams.

In each plot, there exists a region where the branching ratio becomes very small.[1] This is due to the cancellation explained in section II. The positions of cancellation point are fairly close for all plots due to the degenerate slepton masses, but only point A is in the cancellation region and then gives $Br(\mu \to e\gamma)$ below the current experimental upper

---

[1]The difference of the minimum value of the branching ratio in each plot is merely the numerical artifact.
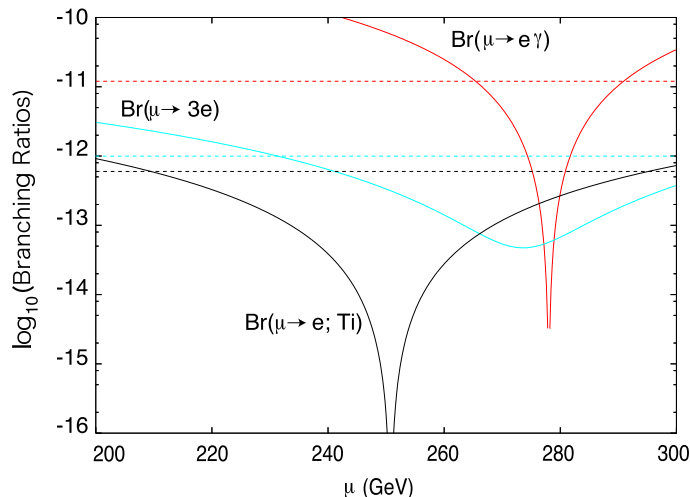
Figure 11. $Br(\mu \to e\gamma)$ (red), $Br(\mu \to 3e)$ (blue) and $Br(\mu \to e; \mathrm{Ti})$ (black) as functions of μ for point A. Here, dashed lines are for the experimental bounds.

bound. Precise determination of μ parameter is then important for determination of flavor mixing parameter, especially for points A and A2 which have similar collider signature but $Br(\mu \to e\gamma)$ differ by two orders of magnitude. In figure 11 we show $Br(\mu \to e\gamma)$, $Br(\mu \to eee)$ and $\mu \to e$ conversion rate in Titanium ($Br(\mu \to e; \mathrm{Ti})$) as functions of μ for point A. The $\mu \to e$ conversion rate from the $Br(\mu \to e\gamma)$ also shows strong sensitivity to the SUSY parameters at different μ values. Because the cancellation takes place in different region, it is important to measure LFV in multiple channels so that we do not miss it accidentally.

We now estimate the error of the SUSY parameters using information from table 4. First of all, we fixed $\tan\beta = 10$ and required that $m_{\tilde\chi_2^0} - m_{\tilde\chi_1^0}$, $m_{\tilde\chi_4^0} - m_{\tilde\chi_1^0}$ and $m_{\tilde\chi_1^0}$ should not differ from their nominal values greater than 1.5 GeV, 2 GeV and 7 GeV respectively. We then looked for the allowed values of M_1, M_2 and μ near their nominal values. Furthermore, we calculated $m_{\tilde e_R}$ and $m_{\tilde e_L}$ using $m_{ll(1)}^{\max}$ and $m_{ll(5)}^{\max}$ information and then calculated $\Delta\chi^2$ defined in eq. (3.4) from other calculated endpoints, i.e. $m_{jll}^{\max}, m_{jl}^{\max}, m_{jl}^{\min}, m_{ll(3)}^{\max}$ and $m_{ll(4)}^{\max}$. The central values of μ, M_1 and M_2 and their ratios are given with their estimated statistical errors within $\Delta\chi^2 = 1$ (1-σ) region in table 13. The absolute values receive sizable errors while the the ratios gives a better sensitivity due to correlation among parameters. Comparing figures 10 and 11, we can see that the size of error of μ is small enough to resolve the position of the cancellation in $Br(\mu \to e\gamma)$.[2]

Even if μ is in the region where $Br(\mu \to e\gamma)$ is canceled, the direct slepton mass measurement at the LHC would provide the information on the non-universality in the slepton mass matrices. As had been emphasized earlier, $m_{\tilde e_R}$ will be measured precisely. Then if $m_{\tilde e_R}$ and $m_{\tilde\mu_R}$ are different due to the flavor violating effect, we will measure each of them rather accurately. In addition, the error in $m_{\tilde e, \tilde\mu} - m_{\tilde\chi_1^0}$ in table 7 tends to cancel when we take the difference $m_{\tilde e_{R(L)}} - m_{\tilde\mu_{R(L)}}$. We therefore estimate errors of slepton mass

---

[2]Since information of μ is obtained mainly from $m_{\tilde\chi_4^0}$, it would not be so sensitive to $\tan\beta$. In addition, the cancellation point of $Br(\mu \to e\gamma)$, eq. (2.17) is insensitive to $\tan\beta$ neither.

Parameter	Central value	Estimated error
μ	271.33	$+6.89$ -6.81
M_1	122.49	$+7.16$ -7.17
M_2	230.89	$+6.57$ -6.54
μ/M_1	2.215	$+0.084$ -0.078
M_2/M_1	1.885	$+0.063$ -0.057

Table 13. Central values and 1-σ constrained intervals of μ, M_1 and M_2 and their ratios after constraints from various cascade decay endpoints are imposed as described in the text.

Mass difference	Central value	Estimated error
$m_{\tilde{e}_R} - m_{\tilde{\mu}_R}$	1.00	$+0.04$ -0.04
$m_{\tilde{e}_L} - m_{\tilde{\mu}_L}$	2.00	$+0.48$ -0.49

Table 14. One-σ error estimation of mass splitting between selectron and smuon in GeV when $m_{\tilde{e}_R} - m_{\tilde{\mu}_R} = 1\,\mathrm{GeV}$ and $m_{\tilde{e}_L} - m_{\tilde{\mu}_L} = 2\,\mathrm{GeV}$ are assumed.

difference in table 14 by assuming $m_{\tilde{e}_R} - m_{\tilde{\mu}_R} = 1\,\mathrm{GeV}$ and $m_{\tilde{e}_L} - m_{\tilde{\mu}_L} = 2\,\mathrm{GeV}$.

By taking μ, M_1 and M_2 of our model point A and assuming flavor-violating parameters as the model with horizontal symmetry described in section II, mass difference $m_{\tilde{e}_R} - m_{\tilde{\mu}_R}$ and $Br(\mu \to e\gamma)$ are plotted as a function of parameter x in figure 12. Note that since LFV masses in the left-handed slepton sector are highly suppressed in this model, then left-handed smuon-selectron mass splitting is predicted to be undetectable for this case. The current experimental bound by MEGA [19] and the MEG sensitivity [22] are also displayed. The mass difference of order one percent, corresponding to $1 \sim 2\,\mathrm{GeV}$, is allowed by MEGA bound due to the partial cancellation. Even though the statistical error of $m_{\tilde{e}_R} - m_{\tilde{\mu}_R}$ in table 14 are very good, however from the fact that slepton decay width is around $0.2\,\mathrm{GeV}$, we simply expect that the LHC has roughly equal sensitivity to the MEG experiment.

A similar plot for the MSSM with right-handed neutrinos is shown in figure 13. In this model, the left-handed smuon and stau are mixed and form the lighter/heavier state $\tilde{l}_{1/2L}$. The horizontal axis now represents common right-handed neutrino mass scale. We show $Br(\tau \to \mu\gamma)$ because it gives the most stringent bound in this model. The experimental bounds of BABAR and Belle [57] allow mass splitting between left-handed selectron and $\tilde{l}_{1L}$ of order few GeV.

As mentioned before, point A is in the cancellation region and simultaneously provides an acceptable dark matter relic density. This can be understood by the followings. In figure 14, we plotted values of $\mu, m_{\tilde{e}_R}, m_{\tilde{e}_L}, m_{\tilde{\chi}_2^0}$, and $m_{\tilde{\chi}_4^0}$ as functions of m_0 when $m_{1/2}$ is fixed at $300\,\mathrm{GeV}$ and $\tan\beta = 10$. In the plot, we assume the mSUGRA relation among slepton and gaugino masses:
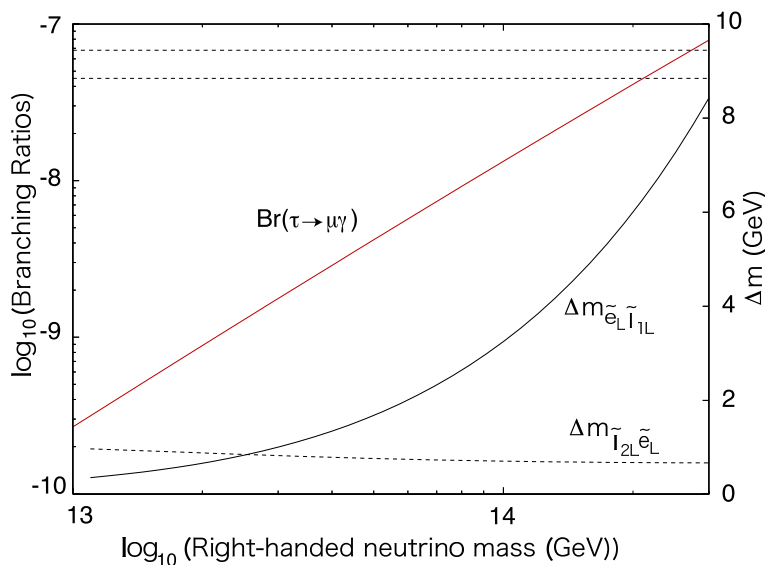
$$M_1 = 0.4 m_{1/2}, \qquad M_2 = 0.8 m_{1/2}, \tag{5.1}$$

$$m_{\tilde{l}_L}^2 = m_0^2 + 0.5 m_{1/2}^2 - \left(\frac{1}{2} - \sin^2\theta_W\right) m_Z^2 \cos 2\beta, \tag{5.2}$$

$$m_{\tilde{l}_R}^2 = m_0^2 + 0.15 m_{1/2}^2 - \sin^2\theta_W m_Z^2 \cos 2\beta, \tag{5.3}$$
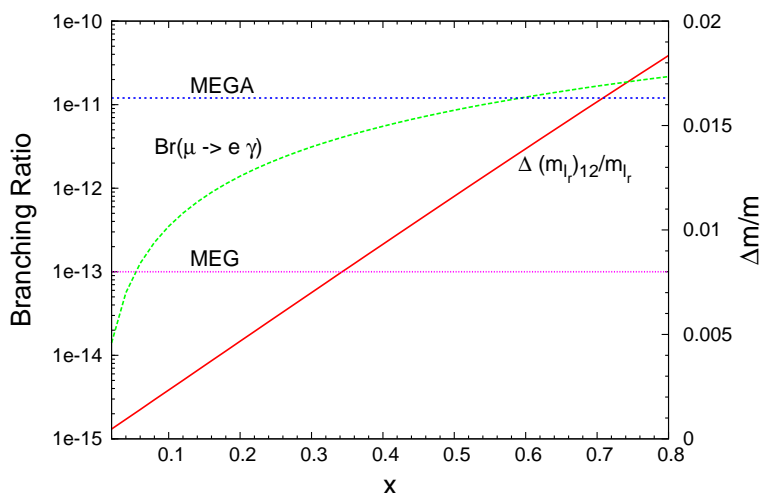
Figure 12. Mass splitting $\Delta(m_{\tilde{l}_R})_{12}/m_{\tilde{l}_R} \equiv 2(m_{\tilde{e}_R} - m_{\tilde{\mu}_R})/(m_{\tilde{e}_R} + m_{\tilde{\mu}_R})$ and $Br(\mu \to e\gamma)$ in the model with horizontal symmetry as a function of parameter x. The current experimental bound and the MEG sensitivity for $\mu \to e\gamma$ are displayed by horizontal lines.

Figure 13. Mass splittings, $(m_{\tilde{e}_L} - m_{\tilde{l}_{1L}})$ and $(m_{\tilde{l}_{2L}} - m_{\tilde{e}_L})$, and $Br(\tau \to \mu\gamma)$ in the MSSM with right-handed neutrinos as a function of common right-handed neutrino scale. $\tilde{l}_{1/2L}$ is the lighter/heavier mixed state of left-handed smuon and stau. Dashed lines are BABAR and Belle bounds on $Br(\tau \to \mu\gamma)$.

and the value of μ is obtained from the cancellation condition shown in eq. (2.17). The condition requires $\mu \sim m_{\tilde{l}_L}$. Therefore as m_0 increases, μ increases as well. The DM density also increases because Higgsino component of LSP is reduced and scalar masses are increased simultaneously. When m_0 reaches value around $150\,\mathrm{GeV}$, $\Omega_{\mathrm{DM}}h^2 \sim 0.37$. In addition, the decay $\tilde{\chi}_2^0 \to \tilde{e}_R$ is no longer open and the slepton information may be
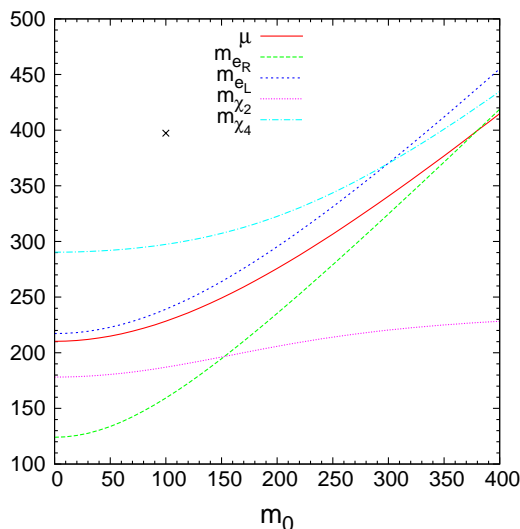
Figure 14. Various sparticle masses and μ value as functions of m_0 at fixed $m_{1/2} = 300\,\mathrm{GeV}$. A cross mark represents μ value of mSUGRA point at $m_0 = 100\,\mathrm{GeV}$.

	$\Omega_{\mathrm{DM}}h^2$	$\sigma_{p\chi}^{SI}(10^{-8}\ pb)$
A	0.1179	1.55
A2	0.0817	3.15
A3	0.0096	17.50

Table 15. Dark matter relic density and spin independent LSP-proton scattering cross section for points A, A2 and A3.

lost. On the other hand, in a small μ region, DM relic abundance is small and $\tilde{\chi}_4^0 \to \tilde{e}_L$ and $\tilde{\chi}_2^0 \to \tilde{e}_R$ are always kinematically allowed. In the case, the possibility to access to both right- and left-handed slepton masses at the LHC is opened if their couplings are not so small. In the same plot, a cross mark represents actual μ value for mSUGRA point at $m_0 = 100\,\mathrm{GeV}$. Besides having too large DM abundance, it is very far from the cancellation point for $Br(\mu \to e\gamma)$. By reducing μ from mSUGRA scenario, the acceptable relic density and $\mu \to e\gamma$ cancellation conditions can be met concurrently.

Finally we comment on the dark matter direct detection cross section of our model points. The DM density and spin independent LSP-proton scattering cross section, $\sigma_{p\chi}^{SI}$, are evaluated for points A, A2 and A3 (table 15). Points A2 and A3 are ruled out by relic abundance if only one species of DM is assumed. Moreover, Point A3 seems to be ruled out already by the recent direct detection bound from CDMS, $\sigma_{p\chi}^{SI} < 4.6 \times 10^{-8}\ pb$ [55]. However, uncertainty in $\sigma_{p\chi}^{SI}$ is large due to three important sources. The first one comes from nucleon matrix element of strange quark, i.e. $\langle p|m_s \bar{s}s|p \rangle$, whose recent calculation was found to be an order of magnitude smaller than the previous ones [56]. Another two sources are $\tan\beta$ and pseudo-scalar Higgs mass, m_A. The pseudo-scalar Higgs exchange diagram gives important contribution proportional to $\left(\frac{\tan^2\beta}{m_A^4}\right)$. In our analysis, we just take $\tan\beta = 10$ and do not fix m_A. However, if the pseudo-scalar Higgs is heavier or $\tan\beta$ has a smaller value

μ/M_1	$\Omega_{\mathrm{DM}}h^2$	$\sigma_{p\chi}^{SI}(10^{-8}\ pb)$
1-σ	0.1101 - 0.1271	1.37 - 1.76
3-σ	0.0929 - 0.1498	1.02 - 2.33

Table 16. Dark matter relic density and spin independent LSP-proton scattering cross section within 1-σ and 3-σ deviations of the μ/M_1 from its nominal value. Here, we assume point A.

than our sample point, the $\sigma_{p\chi}^{SI}$ would become smaller and evade the direct detection bound.

We also show in table 16 the sensitivity of $\Omega_{\mathrm{DM}}h^2$ and $\sigma_{p\chi}^{SI}$ to μ/M_1 ratio for point A. We assumed NUHM with $m_{H_U} \neq m_0$ and changed m_{H_U} value so that μ/M_1 deviates from its central value by 1-σ and 3-σ respectively. The uncertainty of $\sigma_{p\chi}^{SI}$ is larger than that of $\Omega_{\mathrm{DM}}h^2$ unless we fix m_A and $\tan\beta$. Although we assume rather good determination of μ/M_1 ratio, the uncertainty in $\sigma_{p\chi}^{SI}$ is not small, i.e. nearly factor 1.5 for 1-σ.

6 Discussion

In this paper, we studied LHC signature of the one-parameter-extended NUHM, $m_{H_U} \neq m_{H_D} = m_0$. The choice of the boundary condition allows the low energy mass spectrum $M_1 < M_2 < \mu \sim m_{1/2}$. In that case, the LSP relic density may be consistent with cosmological and astrophysical observations because pair-annihilation cross section of the lightest neutralino will be enhanced by the Higgsino components. We are especially interested in the region where cancellation among leading contributions to $Br(\mu \to e\gamma)$ occurs in the models with right-handed LFV masses because the prediction of $Br(\mu \to e\gamma)$ depends strongly on the EW parameters. This cancellation occurs in $m_{\tilde{l}} \sim \mu$ region, therefore, we take a model point with $m_{\tilde{\chi}_1^0} < m_{\tilde{e}_R} < m_{\tilde{\chi}_2^0} < m_{\tilde{e}_L} < m_{\tilde{\chi}_4^0}$ as an example. Both the left- and right-handed sleptons can be directly produced via neutralino decays at the model point.

We investigated how well SUSY parameters can be determined at the LHC for this choice of parameters. In the region when $M_1 < M_2 < \mu \sim m_{1/2}$, $\tilde{\chi}_4^0$ and $\tilde{\chi}_2^{\pm}$ are mixed states with rather large Wino components. They are frequently produced from $\tilde{q}_L$ decay and their decay modes into $\tilde{e}_L$ or $\tilde{\nu}_L$ have large branching ratios. If kinematically allowed, $\tilde{e}_L$ would decay dominantly into Wino-like $\tilde{\chi}_2^0$; however, $\tilde{\chi}_4^0$ and Wino-like $\tilde{\chi}_2^0$ also have small Bino component and they could decay into $\tilde{e}_R$. Accordingly, various decay patterns shown in eq. (2.1), are expectable at the LHC, allowing precise mass determination using endpoint method.

However, even all above decay could be measured at the LHC and masses of all sparticle involving in the decay chains would be identified, there are different regions of SUSY parameter space which have mass spectrum consistent with measured end points. This ambiguity mostly occurs in the neutralino sector.

For our model point, we find three solutions with similar mass spectrum but with different ordering of μ, M_1 and M_2 when the relation $M_1 < M_2$ is kept. These three points predict different $Br(\mu \to e\gamma)$ for the same LFV slepton masses. Because the original point is so close to the cancellation point, the prediction could differ by factor of $\mathcal{O}(100)$ among the three points. The thermal relic density $\Omega_{\mathrm{DM}}h^2$ and $\sigma_{p\chi}^{SI}$ also differ by $\mathcal{O}(10)$. However,

we find that the reordering leads to different properties of neutralinos which will clearly reflect in their decay branching ratio. We showed that $Br(\tilde\chi_i \to 2l + X)$, rate of events in two hard jets+missing E_T channel, and charge asymmetry play important role to lift the degeneracy. This is an excellent example of the complementarity of the LHC and the rare decay searches in SUSY studies.

Acknowledgments

A Trilepton and four-lepton distribution in four-lepton events

We have shown in section III that the four-lepton events from $\tilde\chi_4^0 \to \tilde e_L \to \tilde\chi_2^0 \to \tilde e_R \to \tilde\chi_1^0$ is a useful mode particularly when $Br(\tilde\chi_4^0 \to \tilde e_L \to \tilde\chi_2^0)$ is sizable but its m_{ll} edge cannot be seen in two-lepton events. In this appendix, we show $m_{lll'}$ and $m_{lll'l'}$ distributions as a consistency check.

Again, we selected four-lepton events by the cuts:

- exactly two pairs of OSSF leptons where each lepton has $p_T^l > 10\,\text{GeV}$ and $|\eta| < 2.5$,

- four leptons must be composed of exactly one e^+e^- pair and one $\mu^+\mu^-$ pair.

For each event which passes the cuts, we calculated $m_{lll'}$. The cascade decay is expected to have two trilepton endpoints:

(1) One from the upper part of the decay chain, i.e. $\tilde\chi_4^0 \to \tilde e_L \to \tilde\chi_2^0 \to \tilde e_R$. The expected endpoint $m_{lll'}^{\max} = 192.8\,\text{GeV}$.

(2) Another from the lower part of the decay chain, i.e. $\tilde e_L \to \tilde\chi_2^0 \to \tilde e_R \to \tilde\chi_1^0$. The expected endpoint $m_{lll'}^{\max} = 123.9\,\text{GeV}$.

By utilizing the $m_{ll}^{\max} \sim 123\,\text{GeV}$ from $\tilde\chi_4^0 \to \tilde e_L \to \tilde\chi_2^0$ as in section III, one can further find additional constrain on sparticle masses by looking at the endpoint of the $m_{lll'}$ distribution as follows. Principally,

(1) if one requires $m_{ll} < 70.7\,\text{GeV}$ and $71\,\text{GeV} < m_{l'l'} < 123\,\text{GeV}$, one expects to see the trilepton endpoint from the lower part of the decay chain, or

(2) if one requires $m_{l'l'} < 70.7\,\text{GeV}$ and $71\,\text{GeV} < m_{ll} < 123\,\text{GeV}$ instead, the trilepton endpoint from the upper part of the decay chain is expected to show up.
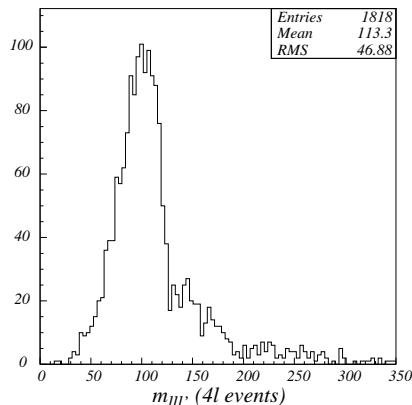
Figure 15. The trilepton invariant mass $m_{lll'}$ distribution (in GeV) which satisfies $m_{ll} < 70.7\,\text{GeV}$ and $71\,\text{GeV} < m_{l'l'} < 123\,\text{GeV}$.
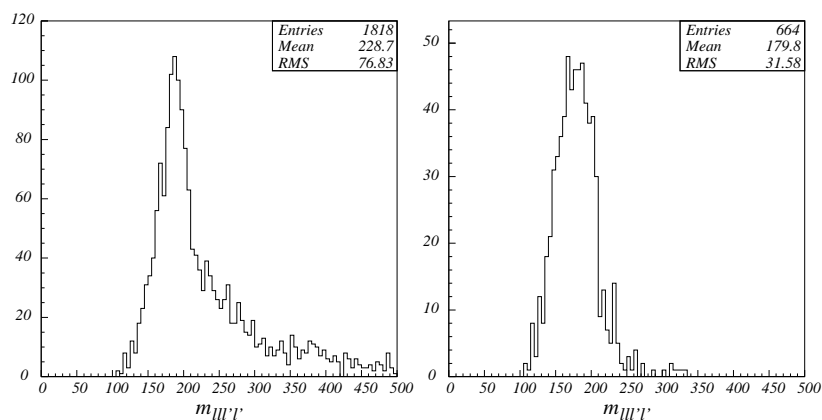
Figure 16. The four-lepton invariant mass $m_{lll'l'}$ distribution (in GeV) satisfying $m_{ll} < 70.7\,\text{GeV}$ and $71\,\text{GeV} < m_{l'l'} < 123\,\text{GeV}$ (left panel). The right panel shows the same distribution when $m_{lll'} < 124\,\text{GeV}$ is further imposed.

However, in our Monte Carlo study, the endpoint from the upper decay chain is invisible. This may be because the distribution for the upper endpoint spreads over wider range so that its height of the peak is lower, and then it is buried under backgrounds. On the contrary, the one from the lower decay chain in figure 15 is rather impressive as it may receive contribution from chargino decay.

Finally, $m_{lll'l'}$ distribution is shown in figure 16. The edge is expected not to exceed the mass difference $m_{\tilde{\chi}_4^0} - m_{\tilde{\chi}_1^0} = 208.5$. In the left panel, m_{ll} of one OSSF pair is required to be $< 70.7\,\text{GeV}$ and that of other OSSF pair is requred to be in the range $71\,\text{GeV} < m_{l'l'} < 123\,\text{GeV}$. Once we further impose the constrain $m_{lll'} < 124\,\text{GeV}$, the tail almost disappears as shown in the right panel.

References

[1] LEP WORKING GROUP FOR HIGGS BOSON SEARCHES collaboration, R. Barate et al., *Search for the standard model Higgs boson at LEP*, *Phys. Lett.* **B 565** (2003) 61 [hep-ex/0306033] [SPIRES].

[2] WMAP collaboration, D.N. Spergel et al., *Wilkinson Microwave Anisotropy Probe (WMAP) three year results: implications for cosmology*, *Astrophys. J. Suppl.* **170** (2007) 377 [`astro-ph/0603449`] [SPIRES].

[3] SDSS collaboration, M. Tegmark et al., *Cosmological constraints from the SDSS luminous red galaxies*, *Phys. Rev.* **D 74** (2006) 123507 [`astro-ph/0608632`] [SPIRES].

[4] WMAP collaboration, D.N. Spergel et al., *First-year Wilkinson Microwave Anisotropy Probe (WMAP) observations: determination of cosmological parameters*, *Astrophys. J. Suppl.* **148** (2003) 175 [`astro-ph/0302209`] [SPIRES];
WMAP collaboration, E. Komatsu et al., *Five-year Wilkinson Microwave Anisotropy Probe (WMAP) observations: cosmological interpretation*, *Astrophys. J. Suppl.* **180** (2009) 330 [`arXiv:0803.0547`] [SPIRES].

[5] SUPERNOVA SEARCH TEAM collaboration, A.G. Riess et al., *Observational evidence from supernovae for an accelerating universe and a cosmological constant*, *Astron. J.* **116** (1998) 1009 [`astro-ph/9805201`] [SPIRES];
SUPERNOVA COSMOLOGY PROJECT collaboration, S. Perlmutter et al., *Measurements of Ω and Λ from 42 high-redshift supernovae*, *Astrophys. J.* **517** (1999) 565 [`astro-ph/9812133`] [SPIRES];
SUPERNOVA SEARCH TEAM collaboration, J.L. Tonry et al., *Cosmological results from high-z supernovae*, *Astrophys. J.* **594** (2003) 1 [`astro-ph/0305008`] [SPIRES];
SUPERNOVA COSMOLOGY PROJECT collaboration, R.A. Knop et al., *New constraints on Ω_M, Ω_Λ and w from an independent set of eleven high-redshift supernovae observed with HST*, *Astrophys. J.* **598** (2003) 102 [`astro-ph/0309368`] [SPIRES];
SUPERNOVA SEARCH TEAM collaboration, A.G. Riess et al., *Type Ia supernova discoveries at $z > 1$ from the Hubble space telescope: evidence for past deceleration and constraints on dark energy evolution*, *Astrophys. J.* **607** (2004) 665 [`astro-ph/0402512`] [SPIRES].

[6] SDSS collaboration, D.J. Eisenstein et al., *Detection of the baryon acoustic peak in the large-scale correlation function of SDSS luminous red galaxies*, *Astrophys. J.* **633** (2005) 560 [`astro-ph/0501171`] [SPIRES].

[7] D. Clowe et al., *A direct empirical proof of the existence of dark matter*, *Astrophys. J.* **648** (2006) L109 [`astro-ph/0608407`] [SPIRES].

[8] J. Ellis and D.V. Nanopoulos, *Flavor changing neutral interactions in broken supersymmetric theories*, *Phys. Lett.* **B 110** (1982) 44 [SPIRES];
J.S. Hagellin, S. Kelley and T. Tanaka, *Supersymmetric flavor changing neutral currents: exact amplitudes and phenomenological analysis*, *Nucl. Phys.* **B 415** (1994) 293 [SPIRES];
F. Gabbiani, E. Gabrielli, A. Masiero and L. Silvestrini, *A complete analysis of FCNC and CP constraints in general SUSY extensions of the standard model*, *Nucl. Phys.* **B 477** (1996) 321 [`hep-ph/9604387`] [SPIRES].

[9] A.H. Chamseddine, R.L. Arnowitt and P. Nath, *Locally supersymmetric grand unification*, *Phys. Rev. Lett.* **49** (1982) 970 [SPIRES];
L.E. Ibáñez, *Locally supersymmetric* SU(5) *grand unification*, *Phys. Lett.* **B 118** (1982) 73 [SPIRES];
K. Inoue, A. Kakuto, H. Komatsu and S. Takeshita, *Aspects of grand unified models with softly broken supersymmetry*, *Prog. Theor. Phys.* **68** (1982) 927 [*Erratum ibid.* **70** (1983) 330] [SPIRES];
L. Álvarez-Gaumé, J. Polchinski and M.B. Wise, *Minimal low-energy supergravity*, *Nucl. Phys.* **B 221** (1983) 495 [SPIRES];

J.R. Ellis, D.V. Nanopoulos and K. Tamvakis, *Grand unification in simple supergravity*, *Phys. Lett.* **B 121** (1983) 123 [SPIRES].

[10] J.R. Ellis, K.A. Olive, Y. Santoso and V.C. Spanos, *Supersymmetric dark matter in light of WMAP*, *Phys. Lett.* **B 565** (2003) 176 [hep-ph/0303043] [SPIRES].

[11] M. Drees and M.M. Nojiri, *The neutralino relic density in minimal $N = 1$ supergravity*, *Phys. Rev.* **D 47** (1993) 376 [hep-ph/9207234] [SPIRES];
K. Griest, *Cross sections, relic abundance and detection rates for neutralino dark matter*, *Phys. Rev.* **D 38** (1988) 2357 [*Erratum ibid.* **D 39** (1989) 3802] [SPIRES];
K.A. Olive and M. Srednicki, *New limits on parameters of the supersymmetric standard model from cosmology*, *Phys. Lett.* **B 230** (1989) 78 [SPIRES].

[12] H. Baer, A. Mustafayev, S. Profumo, A. Belyaev and X. Tata, *Neutralino cold dark matter in a one parameter extension of the minimal supergravity model*, *Phys. Rev.* **D 71** (2005) 095008 [hep-ph/0412059] [SPIRES]; *Direct, indirect and collider detection of neutralino dark matter in SUSY models with non-universal Higgs masses*, *JHEP* **07** (2005) 065 [hep-ph/0504001] [SPIRES];
H. Baer, A. Mustafayev, E.-K. Park and X. Tata, *Collider signals and neutralino dark matter detection in relic-density-consistent models without universality*, *JHEP* **05** (2008) 058 [arXiv:0802.3384] [SPIRES].

[13] J.R. Ellis, K.A. Olive and Y. Santoso, *The MSSM parameter space with non-universal Higgs masses*, *Phys. Lett.* **B 539** (2002) 107 [hep-ph/0204192] [SPIRES];
J.R. Ellis, T. Falk, K.A. Olive and Y. Santoso, *Exploration of the MSSM with non-universal Higgs masses*, *Nucl. Phys.* **B 652** (2003) 259 [hep-ph/0210205] [SPIRES];
J.R. Ellis, K.A. Olive and P. Sandick, *Varying the universality of supersymmetry-breaking contributions to MSSM Higgs boson masses*, *Phys. Rev.* **D 78** (2008) 075012 [arXiv:0805.2343] [SPIRES].

[14] M. Drees et al., *Scrutinizing LSP dark matter at the LHC*, *Phys. Rev.* **D 63** (2001) 035008 [hep-ph/0007202] [SPIRES].

[15] J. Hisano, R. Kitano and M.M. Nojiri, *Slepton oscillation at Large Hadron Collider*, *Phys. Rev.* **D 65** (2002) 116002 [hep-ph/0202129] [SPIRES].

[16] P.D. Jong, *Prospects for SUSY searches in CMS and ATLAS*, *AIP Conf. Proc.* **1078** (2009) 21 [arXiv:0809.3708] [SPIRES].

[17] N. Arkani-Hamed, G.L. Kane, J. Thaler and L.-T. Wang, *Supersymmetry and the LHC inverse problem*, *JHEP* **08** (2006) 070 [hep-ph/0512190] [SPIRES].

[18] R. Lafaye, T. Plehn, M. Rauch and D. Zerwas, *Measuring supersymmetry*, *Eur. Phys. J.* **C 54** (2008) 617 [arXiv:0709.3985] [SPIRES].

[19] MEGA collaboration, M.L. Brooks et al., *New limit for the family-number non-conserving decay $\mu^+ \rightarrow e^+\gamma$*, *Phys. Rev. Lett.* **83** (1999) 1521 [hep-ex/9905013] [SPIRES].

[20] BELLE collaboration, K. Hayasaka et al., *New search for $\tau \rightarrow \mu\gamma$ and $\tau \rightarrow e\gamma$ decays at Belle*, *Phys. Lett.* **B 666** (2008) 16 [arXiv:0705.0650] [SPIRES].

[21] BABAR collaboration, B. Aubert et al., *Search for lepton flavor violation in the decay $\tau^\pm \rightarrow e^\pm\gamma$*, *Phys. Rev. Lett.* **96** (2006) 041801 [hep-ex/0508012] [SPIRES].

[22] A. Baldini, *Status of the MEG experiment*, *Nucl. Phys. Proc. Suppl.* **B 168** (2007) 334 [SPIRES].

[23] SuperKEKB Physics Working Group collaboration, A.G. Akeroyd et al., *Physics at super B factory*, hep-ex/0406071 [SPIRES].

[24] M. Bona et al., *SuperB: a high-luminosity asymmetric e^+e^- super flavor factory. Conceptual design report*, arXiv:0709.0451 [SPIRES].

[25] B.C. Allanach, J.P. Conlon and C.G. Lester, *Measuring smuon-selectron mass splitting at the CERN LHC and patterns of supersymmetry breaking*, *Phys. Rev.* **D 77** (2008) 076006 [arXiv:0801.3666] [SPIRES].

[26] M. Hirsch, S. Kaneko and W. Porod, *Supersymmetric seesaw type-II: lHC and lepton flavour violating phenomenology*, *Phys. Rev.* **D 78** (2008) 093004 [arXiv:0806.3361] [SPIRES].

[27] J. Hisano, T. Moroi, K. Tobe and M. Yamaguchi, *Lepton-flavor violation via right-handed neutrino Yukawa couplings in supersymmetric standard model*, *Phys. Rev.* **D 53** (1996) 2442 [hep-ph/9510309] [SPIRES].

[28] K. Griest, M. Kamionkowski and M.S. Turner, *Supersymmetric dark matter above the W mass*, *Phys. Rev.* **D 41** (1990) 3565 [SPIRES].

[29] Muon G-2 collaboration, G.W. Bennett et al., *Final report of the muon E821 anomalous magnetic moment measurement at BNL*, *Phys. Rev.* **D 73** (2006) 072003 [hep-ex/0602035] [SPIRES].

[30] K. Hagiwara, A.D. Martin, D. Nomura and T. Teubner, *Improved predictions for g-2 of the muon and $\alpha_{\rm QED}(M_Z^2)$*, *Phys. Lett.* **B 649** (2007) 173 [hep-ph/0611102] [SPIRES].

[31] M. Passera, W.J. Marciano and A. Sirlin, *The muon g-2 and the bounds on the Higgs boson mass*, *Phys. Rev.* **D 78** (2008) 013009 [arXiv:0804.1142] [SPIRES].

[32] F. Borzumati and A. Masiero, *Large muon and electron number violations in supergravity theories*, *Phys. Rev. Lett.* **57** (1986) 961 [SPIRES].

[33] J. Hisano and D. Nomura, *Solar and atmospheric neutrino oscillations and lepton flavor violation in supersymmetric models with the right-handed neutrinos*, *Phys. Rev.* **D 59** (1999) 116005 [hep-ph/9810479] [SPIRES].

[34] J. Hisano and K. Tobe, *Neutrino masses, muon g-2 and lepton-flavour violation in the supersymmetric see-saw model*, *Phys. Lett.* **B 510** (2001) 197 [hep-ph/0102315] [SPIRES].

[35] C.D. Froggatt and H.B. Nielsen, *Hierarchy of quark masses, Cabibbo angles and CP-violation*, *Nucl. Phys.* **B 147** (1979) 277 [SPIRES].

[36] M. Leurer, Y. Nir and N. Seiberg, *Mass matrix models: the sequel*, *Nucl. Phys.* **B 420** (1994) 468 [hep-ph/9310320] [SPIRES].

[37] Y. Grossman and Y. Nir, *Lepton mass matrix models*, *Nucl. Phys.* **B 448** (1995) 30 [hep-ph/9502418] [SPIRES].

[38] J.L. Feng, C.G. Lester, Y. Nir and Y. Shadmi, *The standard model and supersymmetric flavor puzzles at the Large Hadron Collider*, *Phys. Rev.* **D 77** (2008) 076002 [arXiv:0712.0674] [SPIRES].

[39] J. Hisano, T. Moroi, K. Tobe and M. Yamaguchi, *Exact event rates of lepton flavor violating processes in supersymmetric SU(5) model*, *Phys. Lett.* **B 391** (1997) 341 [*Erratum ibid.* **B 397** (1997) 357] [hep-ph/9605296] [SPIRES].

[40] R. Kitano, M. Koike and Y. Okada, *Detailed calculation of lepton flavor violating muon electron conversion rate for various nuclei*, *Phys. Rev.* **D 66** (2002) 096002 [*Erratum ibid.* **D 76** (2007) 059902] [hep-ph/0203110] [SPIRES].

[41] F.E. Paige, S.D. Protopopescu, H. Baer and X. Tata, *ISAJET* 7.69: *a Monte Carlo event generator for pp, p̄p and e^+e^- reactions*, hep-ph/0312045 [SPIRES].

[42] H. Baer, C. Balázs and A. Belyaev, *Neutralino relic density in minimal supergravity with co-annihilations*, *JHEP* **03** (2002) 042 [hep-ph/0202076] [SPIRES].

[43] G. Corcella et al., *HERWIG* 6.5: *an event generator for hadron emission reactions with interfering gluons (including supersymmetric processes)*, *JHEP* **01** (2001) 010 [hep-ph/0011363] [SPIRES].

[44] E. Richter-Was, *AcerDET: a particle level fast simulation and reconstruction package for phenomenological studies on high p_T physics at LHC*, hep-ph/0207355 [SPIRES].

[45] I. Hinchliffe, F.E. Paige, M.D. Shapiro, J. Soderqvist and W. Yao, *Precision SUSY measurements at CERN LHC*, *Phys. Rev.* **D 55** (1997) 5520 [hep-ph/9610544] [SPIRES].

[46] H. Bachacou, I. Hinchliffe and F.E. Paige, *Measurements of masses in SUGRA models at CERN LHC*, *Phys. Rev.* **D 62** (2000) 015009 [hep-ph/9907518] [SPIRES].

[47] B.C. Allanach, C.G. Lester, M.A. Parker and B.R. Webber, *Measuring sparticle masses in non-universal string inspired models at the LHC*, *JHEP* **09** (2000) 004 [hep-ph/0007009] [SPIRES].

[48] B.K. Gjelsten, D.J. Miller and P. Osland, *Measurement of SUSY masses via cascade decays for SPS* 1a, *JHEP* **12** (2004) 003 [hep-ph/0410303] [SPIRES].

[49] LHC/LC STUDY GROUP collaboration, G. Weiglein et al., *Physics interplay of the LHC and the ILC*, *Phys. Rept.* **426** (2006) 47 [hep-ph/0410364] [SPIRES].

[50] A.J. Barr, *Determining the spin of supersymmetric particles at the LHC using lepton charge asymmetry*, *Phys. Lett.* **B 596** (2004) 205 [hep-ph/0405052] [SPIRES].

[51] T. Goto, K. Kawagoe and M.M. Nojiri, *Study of the slepton non-universality at the CERN Large Hadron Collider*, *Phys. Rev.* **D 70** (2004) 075016 [*Erratum ibid.* **D 71** (2005) 059902] [hep-ph/0406317] [SPIRES].

[52] C.G. Lester and D.J. Summers, *Measuring masses of semiinvisibly decaying particles pair produced at hadron colliders*, *Phys. Lett.* **B 463** (1999) 99 [hep-ph/9906349] [SPIRES]; A. Barr, C. Lester and P. Stephens, m_{T2}: *the truth behind the glamour*, *J. Phys.* **G 29** (2003) 2343 [hep-ph/0304226] [SPIRES].

[53] ATLAS collaboration, G. Aad et al., *Expected performance of the ATLAS experiment — detector, trigger and physics*, CERN-OPEN-2008-020 [arXiv:0901.0512] [SPIRES].

[54] W.S. Cho, K. Choi, Y.G. Kim and C.B. Park, *Measuring superparticle masses at hadron collider using the transverse mass kink*, *JHEP* **02** (2008) 035 [arXiv:0711.4526] [SPIRES].

[55] CDMS collaboration, Z. Ahmed et al., *Search for weakly interacting massive particles with the first five-tower data from the cryogenic dark matter search at the Soudan underground laboratory*, *Phys. Rev. Lett.* **102** (2009) 011301 [arXiv:0802.3530] [SPIRES].

[56] JLQCD collaboration, H. Ohki et al., *Nucleon sigma term and strange quark content from lattice QCD with exact chiral symmetry*, *Phys. Rev.* **D 78** (2008) 054502 [arXiv:0806.4744] [SPIRES].

[57] S. Banerjee, *Searches for lepton flavor violating decays $\tau^\pm \to \ell^\pm\gamma$, $\tau^\pm \to \ell^\pm$ P0 (where $\ell^- = e^-$, μ^- and P0 = π^0, η, η') at B^- factories: status and combinations*, *Nucl. Phys. Proc. Suppl.* **169** (2007) 199 [hep-ex/0702017] [SPIRES].